Economic Geology, v. XXX, no. XX, pp. X–X

Genesis of the 1.45 Ga Kratz Spring Iron Oxide-Apatite Deposit Complex in Southeast Missouri, USA: Constraints from Oxide Mineral Chemistry

Brandon Sullivan,[1] Marek Locmelis,[1,†] Bolorchimeg N. Tunnell,[2] Cheryl Seeger,[3] Marilena Moroni,[4] Sarah Dare,[5] Ryan Mathur,[6] and Thomas Schott[7]

[1] *Department of Geosciences and Geological and Petroleum Engineering, Missouri University of Science and Technology, Rolla, Missouri 65409, USA*

[2] *Department of Geology and Hydrogeology, School of Geology and Mining Engineering, Mongolian University of Science and Technology, Ulaanbaatar, Mongolia*

[3] *Missouri Department of Natural Resources, Missouri Geological Survey, USA*

[4] *Department of Earth Sciences, University of Milan, Italy*

[5] *Département de Sciences Appliquées, Université du Québec á Chicoutimi, Québec G7H 2B1, Canada*

[6] *Juniata College, 1700 Moore St, Huntingdon, Pennsylvania 16652, USA*

[7] *Exploration and Development, The Doe Run Company, Viburnum, Missouri*

Abstract

The U.S. state of Missouri contains seven major and numerous lesser Fe oxide deposits within the 1.47 Ga St. Francois Mountains terrane. These deposits have been previously described as iron oxide-apatite (IOA) and iron oxide-copper-gold (IOCG) deposits and are speculated to contain significant resources of critical minerals, most notably rare earth elements and cobalt. One of the less-studied deposits in the region is the 1.455 Ga Kratz Spring deposit. The deposit consists of two steeply dipping magnetite bodies beneath 450 m of sedimentary cover. The genesis of the Kratz Spring deposit and its relationship to nearby IOA-IOCG deposits remains poorly constrained. To better understand the formation of the Kratz Spring deposit, we integrated stratigraphic, petrographic, and bulk rock studies with in situ trace element and Fe isotope chemistry of magnetite and hematite. Our data show that the Kratz Spring deposit is hydrothermal in origin but is divided into two subdeposits according to different fluid sources and formation conditions: (1) a deep but cooler hydrothermal Kratz Spring South deposit with a juvenile fluid source and (2) a shallow but hotter magmatic-hydrothermal Kratz Spring North deposit with variable fluid sources. Our genetic model suggests the two Kratz Spring deposits are local expressions of the same mineralization system; i.e., the Kratz Spring South deposit is a distal, lower-temperature offshoot of the feeder system that formed the Kratz Spring North deposit. Understanding the magmatic-hydrothermal plumbing system that formed Missouri's IOA-IOCG deposits is important to guide critical mineral exploration efforts in the region.

Introduction

Southeast Missouri, U.S.A., contains seven major and five lesser iron oxide deposits hosted within the 1.3 to 1.5 Ga granites and rhyolites of the St. Francois Mountains terrane (Day et al., 2016). Some deposits, such as the Pilot Knob surface hematite, Pilot Knob underground magnetite, Iron Mountain, and Cedar Hill deposits, crop out or are near the surface and were discovered and then mined in the 19th century (Starkey and Seeger, 2016). Other deposits on the western edge of the St. Francois, such as the Kratz Spring, Pea Ridge, Boss, and Bourbon deposits, are covered by more than 400 m of sedimentary rock and were discovered via aeromagnetic surveys and drilling in the 1940s and 1950s (Day et al., 2016; Starkey and Seeger, 2016). Of the deeper deposits to the west, overlain by sedimentary rocks, only Pea Ridge was mined from 1963 to 2001 (Starkey and Seeger, 2016).

Several of Missouri's granite/rhyolite-hosted iron deposits have been mineralogically and geochemically characterized and consequently were broadly divided into two groups based on sulfide contents and Ti concentrations in oxide minerals. For example, the iron oxide deposits at Lower Pilot Knob (Tunnell et al., 2021) and Pea Ridge (Day et al., 2016) are sulfide poor and are characterized by Ti contents in bulk rock between 0.5 and 4 wt % TiO_2. These deposits are also phosphate rich (i.e., <0.5 wt % P_2O_5) and thus were classified as iron oxide-apatite (IOA) deposits by several authors (Childress et al., 2016; Day et al., 2016; Huang et al., 2019; Watts and Mercer, 2020). Pea Ridge also has been uniquely characterized as an iron oxide-apatite–rare earth element (IOA-REE) deposit due to its significant resources of rare earth elements (Mercer et al., 2020). Conversely, deposits such as Boss, that are sulfide rich and have low Ti bulk rock contents (i.e., <0.5 wt % TiO_2), were classified as iron oxide-copper-gold (IOCG) deposits (Seeger, 2000; Day et al., 2016; Mercer et al., 2020). Several other deposits in southeast Missouri, such as Bourbon, Camels Hump, and Kratz Spring, remain poorly characterized, and it remains unclear if they are IOA or IOCG deposits. Determining if these deposits are of IOA or IOCG affinity is crucial to understanding their economic and critical mineral potential.

[†]Corresponding author: e-mail, locmelism@mst.edu

ISSN 0361-0128; doi:10.5382/econgeo.5003; 27 p.
Digital appendices are available in the online Supplements section.

Submitted: March 28, 2022/Accepted: October 19, 2022

IOA deposits tend to occur in back-arc subduction or postorogenic-extension–related terranes and are characterized by massive iron oxides, predominantly as magnetite with lesser hematite and variable amounts of phosphates, most notably apatite, xenotime, and monazite (Nold et al., 2014; Day et al., 2016; Huang et al., 2019). Similar subduction or postsubduction extension tectonic activity has been suggested to have been ongoing during the Mesoproterozoic in southeast Missouri, contemporaneous with IOA and IOCG deposit formation and regional-scale metasomatism (Watts and Mercer, 2020; du Bray et al., 2021; Tunnell et al., 2021, 2022). Although Missouri's IOA deposits were initially thought to be either purely magmatic (Kisvarsanyi and Proctor, 1967) or hydrothermal in origin (Sidder et al., 1993), new models have emerged that suggest IOA deposits worldwide formed primarily through magmatic-hydrothermal to magmatically derived hydrothermal processes based on iron and oxygen isotope geochemistry (Jonsson et al., 2013; Childress et al., 2016; Tunnell et al., 2021). Debate continues in Missouri and globally on the importance of both magmatic and hydrothermal mechanisms for the generation of IOA deposits. Furthermore, the nature of the magmatic processes that form IOA deposits remains debated, ranging from exsolution of an immiscible Fe oxide liquid from silicate melts (Nuelle et al., 1991; Hou et al., 2018) to the flotation of initially igneous magnetite via supercritical fluid bubbles exsolved from an ascending melt (Knipping et al., 2015a, b; Childress et al., 2016; Ovalle et al., 2018). One key difference in these two models is the source and significance of hydrothermal features observed in IOA deposits. For example, the silicate-oxide melt immiscibility model would require a wet silicate melt that produces a dry Fe-Ca-P immiscible melt, where any hydrothermal activity in the surrounding rocks would have to be caused by fluids escaping from the wet conjugate silicate melt, or convection-driven circulation of regional brines (Hou et al., 2018; Ovalle et al., 2018; Watts and Mercer, 2020). In the flotation model, hydrothermal features would be created by the fluid exsolution event that facilitated the flotation and subsequent emplacement of magnetite (Ovalle et al., 2018; Simon et al., 2018; Knipping et al., 2019).

IOCG deposits, like IOA deposits, are characterized by massive iron oxide hosted by felsic to intermediate igneous rocks in back-arc or subduction-related terranes (Storey and Smith, 2017). However, as opposed to IOA deposits, IOCG systems contain more significant sulfide mineralization, primarily pyrite and chalcopyrite, with sizable and sometimes economic concentrations of Au and Co (Ehrig et al., 2012; Day et al., 2016). Some IOCG deposits, like Olympic Dam in Australia, are primarily composed of hematite (Ehrig et al., 2012), whereas others, such as Salobo in Brazil (Campo-Rodríguez et al., 2022) and Boss in Missouri (Seeger, 2003), are dominated by magnetite. IOCG deposits are believed to have formed from hydrothermal to magmatic-hydrothermal processes based on trace element chemistry and fluid inclusion studies (Oreskes and Einaudi, 1992; Seeger, 2003; Bastrakov et al., 2007; Skirrow, 2022). Fluid sources for IOCG deposits remain a topic of debate, with models including juvenile fluids (Storey and Smith, 2017; Childress et al., 2020; Del Real et al., 2021) and evaporitic/sedimentary brine sources (Barton and Johnson, 1996; McPhie et al., 2011).

Owing to similarities in mineralogy (i.e., iron oxide-dominated, extensively K-altered, granitic host rocks) and spatial occurrence (subduction-related extensional environments), IOA and IOCG deposits have been proposed to be genetically related (Sillitoe, 2003; Corriveau et al., 2016; Simon et al., 2018), although such a link remains to be fully established. To advance our understanding of the formation of iron ore deposits in southeast Missouri, this study investigates the largely underexplored Kratz Spring deposit in east-central Missouri (Fig. 1).

Geologic setting

The Kratz Spring deposit is located beneath 450 m of Cambrian to Ordovician sedimentary strata, within porphyritic felsic to intermediate rocks of the St. Francois Mountains igneous province (Day et al., 2016). The St. Francois igneous province is part of the larger Eastern Granite-Rhyolite Province, sometimes referenced as the Shawnee domain, which stretches from south-central Missouri eastward to the basement rocks of Illinois, Kentucky, and Indiana (Sims et al., 1987). The Eastern Granite-Rhyolite Province's exposure in Missouri is limited to the St. Francois Mountains; elsewhere, it is overlain by hundreds of meters of sedimentary rocks (Denison et al., 1984). The Eastern Granite-Rhyolite Province is composed of

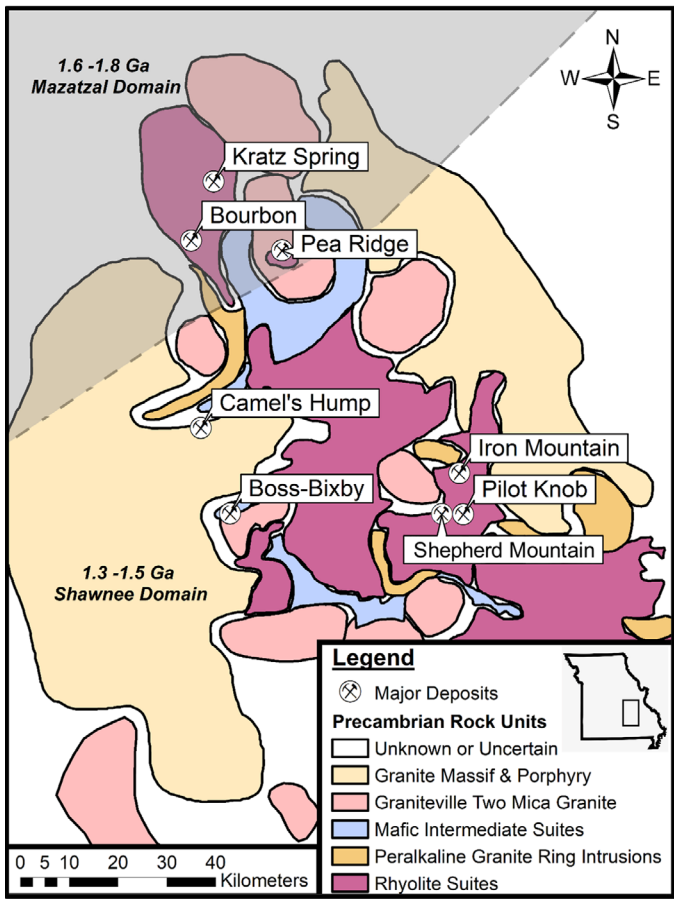

Fig. 1. Geologic map that shows the field area in of the St. Francois Igneous Province modified from Day et al. (2016) using drilling data from The Doe Run Company. The inset shows the location of the map within the U.S. state of Missouri.

A-type rhyolites and granites of peralkaline to peraluminous affinities with minor mafic-intermediate rocks including diabase dikes, gabbroic plutons, and basaltic andesite (Denison et al., 1984). The rhyolites are largely present as ash fall and ash flow tuffs with minor rhyolitic lava flows (Day et al., 2016). The granites are geochemically and texturally variable and include the massif-type Butler Hill seriate granite, the two-mica Graniteville granite, and the hornblende-bearing Silvermines granite (Day et al., 2016). Magmatism in the Eastern Granite-Rhyolite Province occurred as two distinct pulses at 1.47 Ga (associated with most of the rhyolites and the Butler Hill and Silvermines granites) and at 1.3 Ga (associated with the Graniteville granite and most of the diabase dikes; Day et al., 2016). Iron oxide mineralization is more closely linked to the earlier pulse, with ages of emplacement for Pea Ridge (Ayuso et al., 2016; Neymark et al., 2016; Watts and Mercer, 2020), Boss (Aleinikoff, 2021; du Bray et al., 2021), and Pilot Knob Magnetite (Tunnell et al., 2021) all indicated to be between 1.44 and 1.47 Ga.

The formation and evolution of the Eastern Granite-Rhyolite Province have been subject to debate. Due to its A-type geochemical signature, formation mechanisms first proposed reflected anorogenic processes, such as rifting and hot spot activity (Denison et al., 1984; du Bray et al., 2021). More recently, however, studies proposed that orogenic processes had a larger role than previously thought based on immobile trace element data from the Eastern Granite-Rhyolite Province (Day et al., 2016; Tunnell et al., 2021, 2022) and dating of zircons in terrane-wide granitic rocks (Bickford et al., 2015; Watts and Mercer, 2020). These new insights lead to a comparison of the Eastern Granite-Rhyolite Province to similar modern tectonic environments, such as the Basin and Range Province of the western United States, that have been shown to have undergone subduction-related extension (Best et al., 2016), and the Andes (Tornos et al., 2017).

Previous studies on the Kratz Spring deposit

The Kratz Spring deposit in Franklin County, Missouri, (Fig. 1) occurs 20 km to the northwest of the Pea Ridge IOA-REE deposit and 12 km to the northeast of the Bourbon deposit. Drill core descriptions and bulk-rock data suggested that Kratz Spring is an IOA-type deposit (Day et al., 2016). The deposit was drilled by the St. Joseph Lead Corporation between 1954 and 1958 following the discovery of magnetic anomalies during aeromagnetic surveys (Starkey and Seeger, 2016). Later geophysical study by McCafferty et al. (2016) indicates that the Kratz Spring deposit may be divided into two subdeposits: Kratz Spring South and Kratz Spring North (Fig. 2). Barren rock separates the two deposits by approximately 4 km. Previous studies have suggested the deposits are hosted entirely within rhyolites and are crosscut by postmineralization mafic to mafic-intermediate, centimeter- to meter-sized dikes (Day et al., 2016). Apatite in the Kratz Spring deposit was age dated using U-Pb by Moscati and Neymark (2021), with an average age of 1.455 Ga. This age is younger than the 1.474 Ga granite and rhyolite host rocks but distinctly predates the later 1.27 Ga granite and diabase. Other IOA deposits in the region have been age dated using apatite and zircon U-Pb and were shown to be of similar age, i.e., 1.456 to 1.471 Ga at Pea Ridge (Neymark et al., 2016; Watts and Mercer, 2020) and 1.432 to 1.444 Ga at Pilot Knob (Tunnell et al., 2021).

To understand the formation of the Kratz Spring deposit, we conducted the first detailed stratigraphic, petrographic, mineralogical, and mineral-chemical study of this deposit. We establish host rock and iron oxide mineralization domains using new drill core observations, petrographic observations, and bulk rock data. Oxide minerals are characterized using transmitted- and reflected-light microscopy, as well as scanning electron microscope (SEM), electron microprobe (EMPA), laser ablation-inductively coupled plasma-mass spectrometry (LA-ICP-MS), and iron isotope analyses. The data are used to demonstrate that the Kratz Spring deposit is an IOA-style deposit and that the two subdeposits discovered by geophysics, i.e., Kratz Spring North and South, are local expressions of the same hydrothermal system emplaced at different stratigraphic levels.

Methodology

Sampling

Thirty-five half core samples (4.2 cm in diameter) were selected from five diamond drill cores, one from Kratz Spring South and four from Kratz Spring North, owned by The Doe Run Company. The strategy was to sample the different Fe oxide and gangue mineral textures present in the deposits as well as the host-rock lithologies of both subdeposits. Samples were prepared as 2.5-cm polished mounts for reflected-light microscopy and in situ mineral analysis. A subset of seven polished thin sections was also prepared for transmitted-light microscopic studies.

Petrographic studies

Petrographic studies were conducted using a Leica DVM-6 digital microscope at Missouri University of Science and Technology. A subset of six samples was investigated using backscattered electron (BSE) and energy dispersive spectrography (EDS) detectors on Hitachi S4700 and RAITH e-line plus SEMs in the Advanced Materials Characterization Laboratory.

Mineral analysis

The major and minor element composition of amphibole at Kratz Spring was determined using a JEOL JXA-8200 EPMA at Washington University, St. Louis, Missouri. The microprobe is equipped with five wavelength dispersive spectrometers (WDS) with light and trace element detection as well as cathode-luminescence and EDS capabilities. Profiles and spots were collected at 15 kV and 50 nA with a beam size of 5 µm. Calibration and data reduction were conducted using a combination of natural and synthetic standard materials. Mean accuracy and precision were under 1.1 wt % (2σ; cf. App. Table A1.1). Hornblende formulas were calculated using the amphibole nomenclature classification by Leake et al. (1997).

The major element composition of magnetite and hematite was determined at Université Laval, Quebec, Canada, using a Cameca SX-100 EPMA with four WDS units. Data were collected with a beam current of 20 nA with a residence time of 20 s per spot. Calibration and data reduction were conducted using a combination of natural and synthetic standard materi-

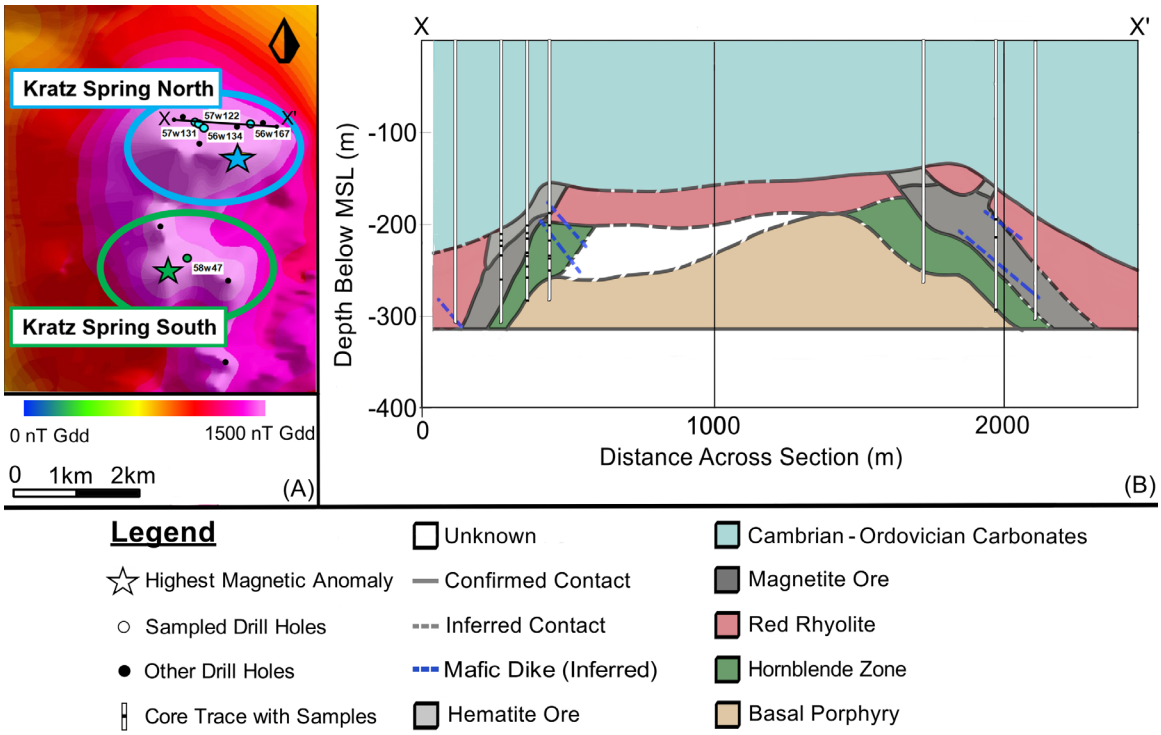

Fig. 2. (A) Plan view of the magnetic anomaly of Kratz Spring modified from McCafferty et al. (2016) with cross section trace (black line) and drill holes sampled in this project (colored); other drill holes into the deposit in the area are black. (B) Cross section of Kratz Spring North, with the Y axis set to mean sea level (MSL) as a datum to account for differences in collar elevation.

als. The median detection limit for FeO was 306 ppm, with a median uncertainty of 1.2 wt % (2σ; cf. App. Table A1.1).

The minor and trace element compositions of magnetite and hematite from six samples were determined via LA-ICP-MS analysis at LabMaTer (Université du Québec à Chicoutimi, Canada), using a Resonetics M-50 193-nm laser unit connected to an Agilent 7900 ICP-MS. The analysis followed the analytical protocol of Dare et al. (2014); additional elements analyzed included Na, K, and the full REE suite. The analyses used a spot size of 75 µm, a repetition rate of 15 Hz, and a fluence of 5 J/cm^2. Iron contents obtained by electron microprobe were used as the internal standard with the GSE-1G reference glass (Jochum et al., 2005) as the calibrant to quantify elemental abundances in magnetite and hematite. The GProbe6 reference glass (Wilson et al., 2012) and the natural magnetite standard BC-28 (Barnes et al., 2004; Dare et al., 2014) were analyzed during each run as unknowns and show that the accuracy is better than 10% of experimental 2σ uncertainty or within-literature stated compositional variation for all analytes with a precision of 5% (2σ; cf. App. Table A1.4). The GLITTER data reduction software (Griffin et al., 2008) was used to process data and exclude silicate and REE-rich phosphate inclusions from the data reduction.

Iron isotope analysis

Oxide mineral concentrates for iron isotope analysis were prepared from 2- to 5-cm portions of quartered drill core that were crushed using an agate mortar and pestle and sieved to a grain size of 125 to 250 µm. The sieved samples were cleaned using ultrasonic distilled water baths and decanting washes to remove microscale adherent particles. The clean samples were dried and put into a distilled water-filled beaker and separated into magnetic and nonmagnetic fractions using a hand magnet on the bottom of the beaker. The nonmagnetic fraction was washed onto filter paper, dried, and handpicked for hematite under a binocular Leica DVM-6 microscope in the Department of Geosciences and Geological and Petroleum Engineering (GGPE) at Missouri S and T. The magnetic fraction was inspected for any signs of hematite or silicate contamination, such as contaminant particles adhering to magnetite, microinclusions, or polyphase grains. Grains that showed evidence for contamination were removed from the samples by handpicking. Submicron-scale mineral inclusions were not observed in BSE imaging, suggesting that inclusions do not make up a significant enough volume of magnetite or hematite to affect their Fe isotope compositions.

Up to 50 mg of ultrapure magnetite and hematite concentrates from Kratz Spring South were digested in 4 mL of heated, ultrapure distilled aqua regia at Juniata College, Pennsylvania. Complete dissolution of samples was confirmed visually. The dissolved magnetite-acid solutions were dried, redissolved, and then purified using a BioRad MP-1 anion exchange resin column following the procedure of Marechal et al. (1999). The purified solutions were analyzed for their Fe isotope composition at Pennsylvania State University, College Station, Pennsylvania, using a Thermo-Scientific Neptune Plus multicollector (MC)-ICP-MS. Instrument parameters and sample introduction procedures were based on protocols of Yesavage et al. (2016). The MC-ICP-MS was set to high-resolution mode, with sample measurements clustered to

3 ppm, which created a signal of 15 V on the Fe peak. Mass bias was considered by utilizing standard to sample to standard bracketing. As such, Fe isotope compositions are presented compared to Institute for Reference Materials and Measurements (IRMM) standard IRMM-014 and are reported in Appendix Table A2. Other in-house and international standards were also used, including SRM-3126a with an accepted δ^{56}Fe value of 0.34 ± 0.1‰ (Yesavage et al., 2016) and HPS-WU with an accepted δ^{56}Fe value of 0.6 ± 0.07‰ (Beard et al., 2003). These standards were used to quantify the analyses' accuracy and precision; the recorded error was within 0.1‰ of the standards with a 2σ confidence interval. The δ^{56}Fe and δ^{57}Fe values show a strong correlation with r^2 = 0.95, indicating mass-dependent fractionation during analysis, as ^{55}Fe becomes depleted as a share of total Fe relative to heavier ^{56}Fe and ^{57}Fe. This correlation in turn indicates analysis and preparation was done correctly (Troll et al., 2019).

Bulk rock analysis

Bulk rock chemistry was determined at Geoscience Laboratories ("Geolabs"), Ontario, Canada, and Activation Laboratories ("Actlabs"), Ontario, Canada. Major element analyses at Geolabs were conducted using X-ray fluorescence (XRF) and with a detection limit of 100 to 60 ppm and a mean 2σ precision uncertainty of 8.6%. Minor and trace element analyses at Geolabs were analyzed via pressure vessel 4-acid digestion solution ICP-MS analysis, and elemental abundances were determined with a detection limit from 2 ppb to 6 ppm, a mean 2σ precision uncertainty of 6.8%, and an accuracy of 5.5% as shown by repeated analysis of the international standard AGV-2. Major element analyses at Actlabs were conducted via Li-B fusion ICP-MS with detection limits for all major elements of <100 ppm, a mean 2σ precision uncertainty of 1.7%, and accuracy error of 2.6% from W-2a standards. Trace elements at Actlabs were determined using multiacid closed-vessel digestion with ICP-MS finish. Detection limits of the minor and trace elements varied from 0.1 to 20 ppm with a 2σ precision uncertainty of better than 12% and an accuracy of 9% based on repeated analysis of the W-2a standard (App. Table A3.1).

Results

Deposit stratigraphy

The two subdeposits identified by geophysical studies, Kratz Spring North and South, were intercepted by drilling. Similar lithological domains were encountered in both subdeposits (Figs. 2, 3). These include, from bottom to top, (1) a phenocryst-rich, two-feldspar basal granite porphyry unit (Fig. 3B), (2) a 20- to 100-m-thick massive to disseminated magnetite zone with accessory specular hematite and apatite (Fig. 3C), (3) a massive to disseminated martitic hematite zone of similar thickness to the magnetite zone (i.e., 20–100 m) with rare relict magnetite cores in martite (Fig. 3D), and (4) a phenocryst-poor, heavily altered red rhyolite that ranges from being fully absent to exceeding 80 m in thickness (Fig. 3E-F). In addition to these deposit-wide lithological domains, other domains appear to be locally restricted based on the drill core data currently available: (1) a hornblende-rich, intensely metasomatized igneous rock unit (hornblende zone) that occurs between the magnetite mineralization and the granite porphyry, forms up to 75-m-thick lenses, and is restricted to the Kratz Spring North deposit; (2) a series of discordant <10-m-thick diabase dikes and dike networks that are only observed in Kratz Spring North; and (3) a pair of 15-m-thick aplite dikes that are equigranular, aphanitic, oxide-free, and salmon-colored and occur within the magnetite domain at Kratz Spring South (Fig. 3C).

The extensive drilling of Kratz Spring North allowed for construction of a cross section, using historic drill logs as well as new logs created during this study, and a vertical datum (mean sea level [MSL]) to account for differences in drill collar elevations (Fig. 2B). This study has revealed that the Kratz Spring North subdeposit is composed of two steeply dipping magnetite bodies. The cross section highlights that the two magnetite bodies appear to form a dome- or syncline-like structure across an east-to-west profile, with the western, higher-grade magnetite body dipping at a steep angle of 45° to 60° to the west and the eastern, lower-grade magnetite body dipping at a shallower angle of 25° to 40° to the east. The basal granite porphyry also follows this apparent structural trend, which is distinctly crosscut by diabase dikes and the Precambrian erosional surface. It is noted that the Kratz Spring South subdeposit is currently too sparsely drilled to allow for the preparation of a cross section.

Ore mineral and host rock petrography

Basal granite porphyry unit: The stratigraphically lowest rock unit encountered in the drill cores is a granite porphyry, located at a depth of greater than –200 m to deeper than –300 m MSL with 30 to 70 vol % of large (>2.5-mm) feldspar phenocrysts in a groundmass of quartz, sericite, and accessory magnetite. Quartz and sericite abundances range from 15 to 40 modal %. Accessory fine-grained magnetite is often concentrated around feldspar phenocrysts (Fig. 4A) but otherwise is rare. Feldspars in this zone are predominantly orthoclase with lesser albite. Albite can be completely replaced by sericite and is often mantled by orthoclase (Fig. 4A) or granophyric intergrowths of orthoclase and quartz (Fig. 4B). At depths greater than 50 m below the upper contact of the granite porphyry, albite shows less destructive sericite alteration in conjunction with more narrow orthoclase rims (Fig. 4C). Rare millimeter-scale veins of epidote crosscut the porphyry unit (no more than one vein per 2 m of drill core).

Hornblende zone: The granite porphyry unit is overlain by a 50- to 75-m-thick zone of hornblende-rich porphyritic rhyolite- to massive hornblende-dominated rocks (Fig. 2B). Xenolithic blocks of this unit, ranging from a few centimeters to tens of meters in size, can be found in the overlying magnetite domain as well as in the basal granite porphyry. Consequently, the upper and lower contacts are gradual rather than sharp. The hornblende zone is dominated by large, green acicular to blocky hornblende grains that are randomly oriented and often exceed 3 mm in the longest direction (Fig. 5A-B). The modal abundance of hornblende in this zone ranges from 90% in hornblende aggregates to 20% in hornblende-rich rhyolite. Hornblende alters to actinolite in fractures and near its rims, as indicated by an absence of Na and Al in EDS element maps (Fig. 5C). Hornblende often contains 20- to 100-µm-long grains of bastnaesite in 10- to 30-µm-thick fracture fills (Fig.

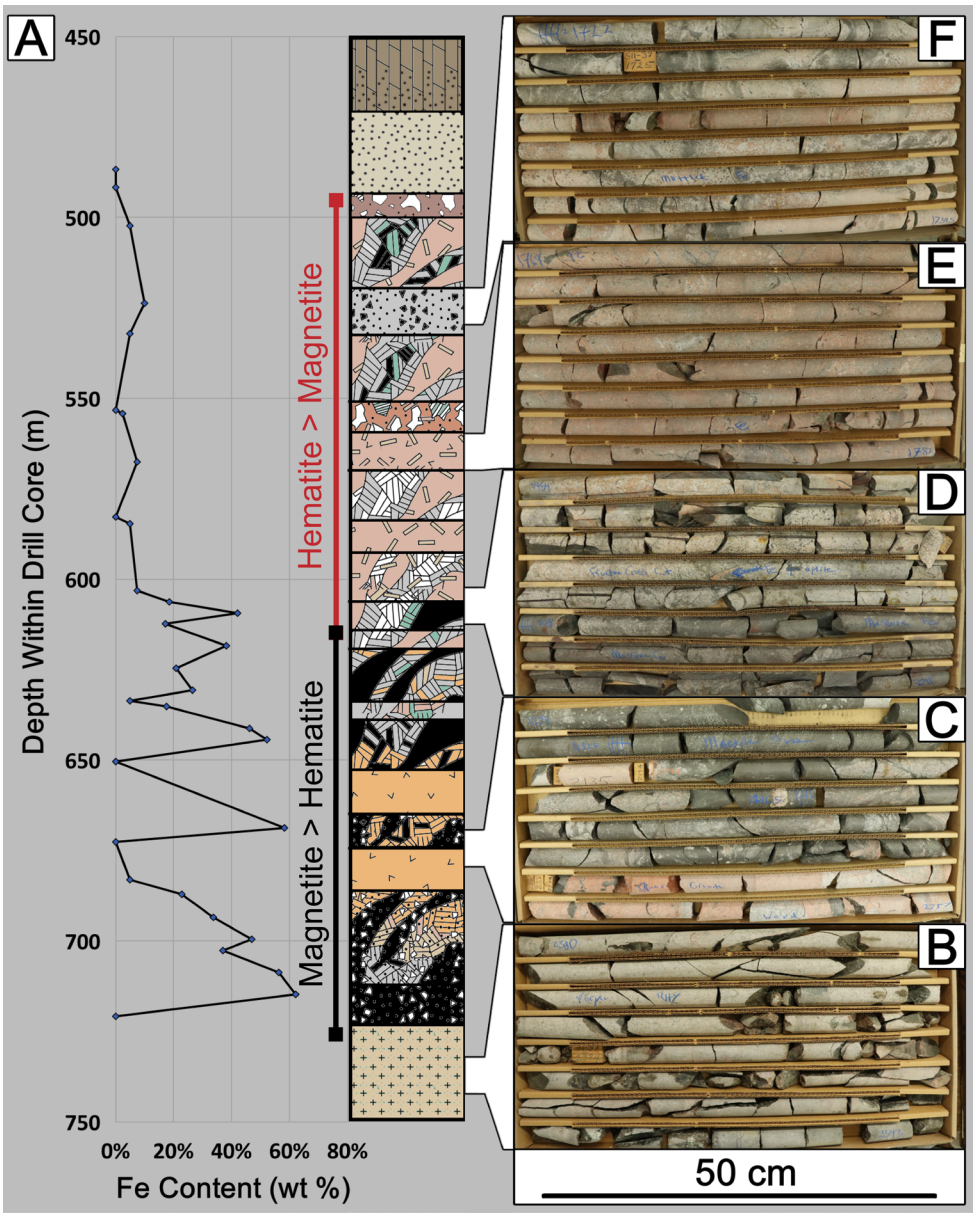

Fig. 3. (A) Historical iron estimate and assay data from The Doe Run Company vs. depth within drill core with artistic (non-symbolic) stratigraphic column of the Kratz Spring South deposit. (B-F) Corresponding images of drill core taken from stratigraphic intervals indicated by white brackets in hole 58W47. (B) Basal granite porphyry unit. (C) Magnetite zone crosscut by salmon-colored aplite. (D) Massive hematite zone below heavily silicified red rhyolite. (E) Red rhyolite with minor magnetite in stringer veins. (F) Red rhyolite with weakly disseminated magnetite/martite.

5D), co-occurring with similarly sized grains of calcite (Fig. 5C) and fluorite (Fig. 5E).

In addition to acicular and blocky hornblende, the hornblende zone also contains large (>1-mm) euhedral biotite grains, most frequently in the thickest intervals of massive hornblende with modal abundances up to 15%. The biotite grains are zoned, with strongly pleochroic yellow to red-brown interiors and paler, yellow-green rims (Fig. 5E). The hornblende zone also contains minor to locally abundant 0.1- to 3-mm-sized grains of fluorite, calcite, and apatite. Calcite within and between hornblende grains is notably transparent (Fig. 5E). In the Kratz Spring North subdeposit, magnetite and specular hematite grains between 1 and 10 mm in size can occur close to, as well as within, the hornblende zone. Magnetite in the hornblende-rich zones is interstitial to hornblende, which commonly displays euhedral hexagonal and elongate crystal forms (Fig. 5F). Specular hematite is anhedral and occurs as open space filling between and around grains of magnetite (Fig. 5G). Apatite is most frequent near the top of the hornblende zones, where it forms massive aggregates and breccias that exceed tens of centimeters in size with apatite modal abundance approaching 95% (Fig. 5H). The apatite aggregates occur as breccia fill and are crosscut by veins that host bastnaesite and calcite. Apatite often exhibits netted fractal vein textures with mineralogy similar to the larger, rock-scale veins (Fig. 5H). It is noted that some isolated apatite

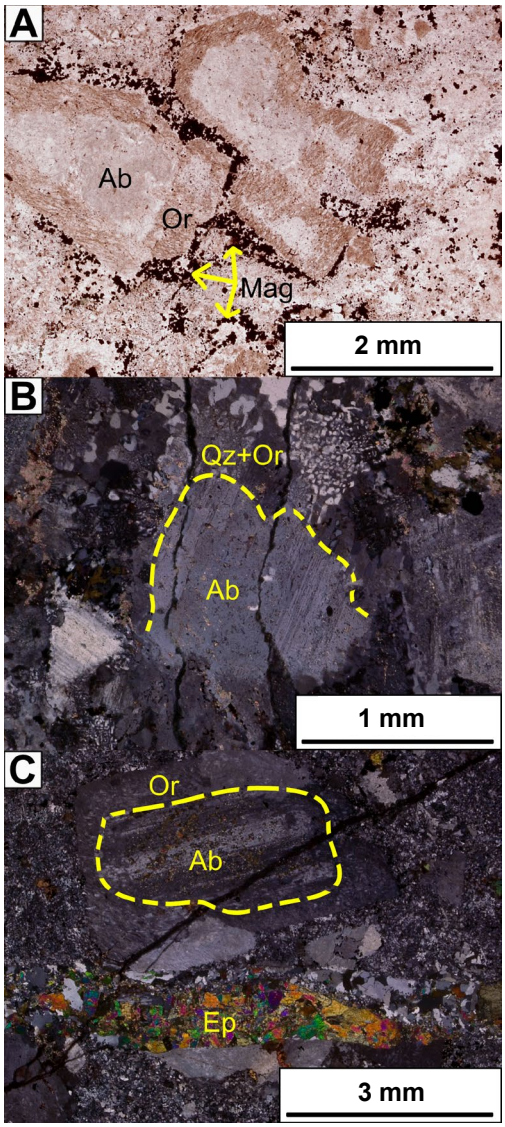

Fig. 4. Representative images of thin sections showing the mineralogy of the basal granite porphyry unit. (A) Transmitted-light image (plane-polarized) Kratz Spring North sample 56W167TL1. (B) Transmitted-light image (cross-polarized) from Kratz Spring South sample 58W47TL13. (C) Transmitted-light image (cross-polarized) from Kratz Spring North sample 57W122TL10. Abbreviations: Ab = albite, Ep = epidote, Mag = magnetite, Or = orthoclase, Qz = quartz.

grains show a faint anhedral mottling, but larger apatite grains are generally dark in backscatter (Fig. 5I).

Magnetite zone: The hornblende zone is overlain by the 35- to 60-m-thick main magnetite zone at Kratz Spring North (Fig. 2B) that is composed of disseminated to massive magnetite. Magnetite modal abundances reach 70 to 95% at the Kratz Spring North magnetite bodies, most commonly as breccia cement and vein fill (Fig. 6B-C). At Kratz Spring North, magnetite occurs massively in vein and fracture networks that crosscut host rock units. Magnetite in these veins occurs as euhedral grains with isolated crystals or as inclusions of hornblende and mottled intergrowths (symplectites) of magnetite, ilmenite, and rutile (Figs. 5I, 6A). Nanometer-scale crosshatch lineations are observed in magnetite at Kratz Spring North; although, because of their submicrometer size, it is unclear if they are exsolutions or possibly strain features (Fig. 6A). The modal abundance of magnetite is 60 to 80% in the Kratz Spring South magnetite zone, and the magnetite zone sits directly atop the lower granite porphyry (Figs. 5I, 6A). The hornblende unit is absent at Kratz Spring South (Fig. 3). In the parts of the magnetite bodies that are closest to the basal porphyry unit at Kratz Spring South, magnetite occurs as micrometer-scale grains that share grain boundaries with anhedral quartz and rutile (Fig. 6B-C). Micron- to millimeter-sized euhedral zircon and rutile grains are randomly dispersed, but locally abundant through the lower magnetite zone. Rutile occurs as isolated crystals with rims of hematite in the Kratz Spring South subdeposit at modal abundances of <15% (Fig. 6B-C). In areas with lower magnetite modal abundances (i.e., <20 modal %) near to or inside the red rhyolite at Kratz Spring South, magnetite can form schlieren-like banding and swirled patterns within highly silicified rock (Fig. 6E).

Magnetite grains become larger and more euhedral with decreasing depth with grain sizes of up to 1.2 mm in diameter at depths exceeding –170 m MSL at Kratz Spring North and –280 m MSL at Kratz Spring South. Sometimes larger magnetite crystals display localized, linear fracture-controlled replacement by martitic hematite (Fig. 6F). Specular hematite locally displays such grains up to 1 mm long and tens of micrometers across (Fig. 6G-H). Apatite at Kratz Spring South occurs in magnetite-rich zones as fine disseminations with micrometer-scale crystals and is commonly associated with specular hematite in chlorite veins and veinlets (Fig. 6H). Grains of pyrite less than 50 µm in diameter are observed within grains of specular hematite at Kratz Spring South. Boundaries between magnetite grains, as well as rims of isolated magnetite, are replaced by martitic hematite, thereby giving massive Fe oxide ores a giraffe pattern-like texture (Fig. 6I). This grain boundary-controlled replacement texture of magnetite with martitic hematite becomes more pervasive with decreasing depth starting at 130 m below the Precambrian-Cambrian unconformity at Kratz Spring South and 70 m below the same unconformity at Kratz Spring North.

Hematite zone: The hematite zone occurs above the magnetite zone in both deposits and is composed of massive to semimassive hematite, with modal abundances of 20 to 60% in Kratz Spring South and 50 to 95% hematite in Kratz Spring North. In both subdeposits, magnetite is progressively replaced by martite above –200 m MSL. Mineralization is dominantly composed of martitic hematite with some sparse relict cores of magnetite up to 100 µm across (Fig. 7A). The most prominent sulfide occurrence in the Kratz Spring deposit was observed in association with martitic hematite and cloudy, translucent calcite and dolomite (Fig. 7B-C), which greatly differs in clarity from the clear calcite observed in hornblende-rich zones described above (Fig. 5E). Sulfide abundances in this zone are generally between 0.5 and 2% and locally up to 5% modal and include pyrite, marcasite, siegenite, and chalcopyrite in decreasing order. Trace amounts of pyrite are also observed elsewhere in the deposit, exclusively as inclusions in oxide mineral grains, predominantly specular hematite (Fig. 6H).

In areas where the Fe oxide zones are shallower (i.e., less than 200 to –150 m MSL), they reach the Precambrian erosional surface and are composed of matrix-supported breccias

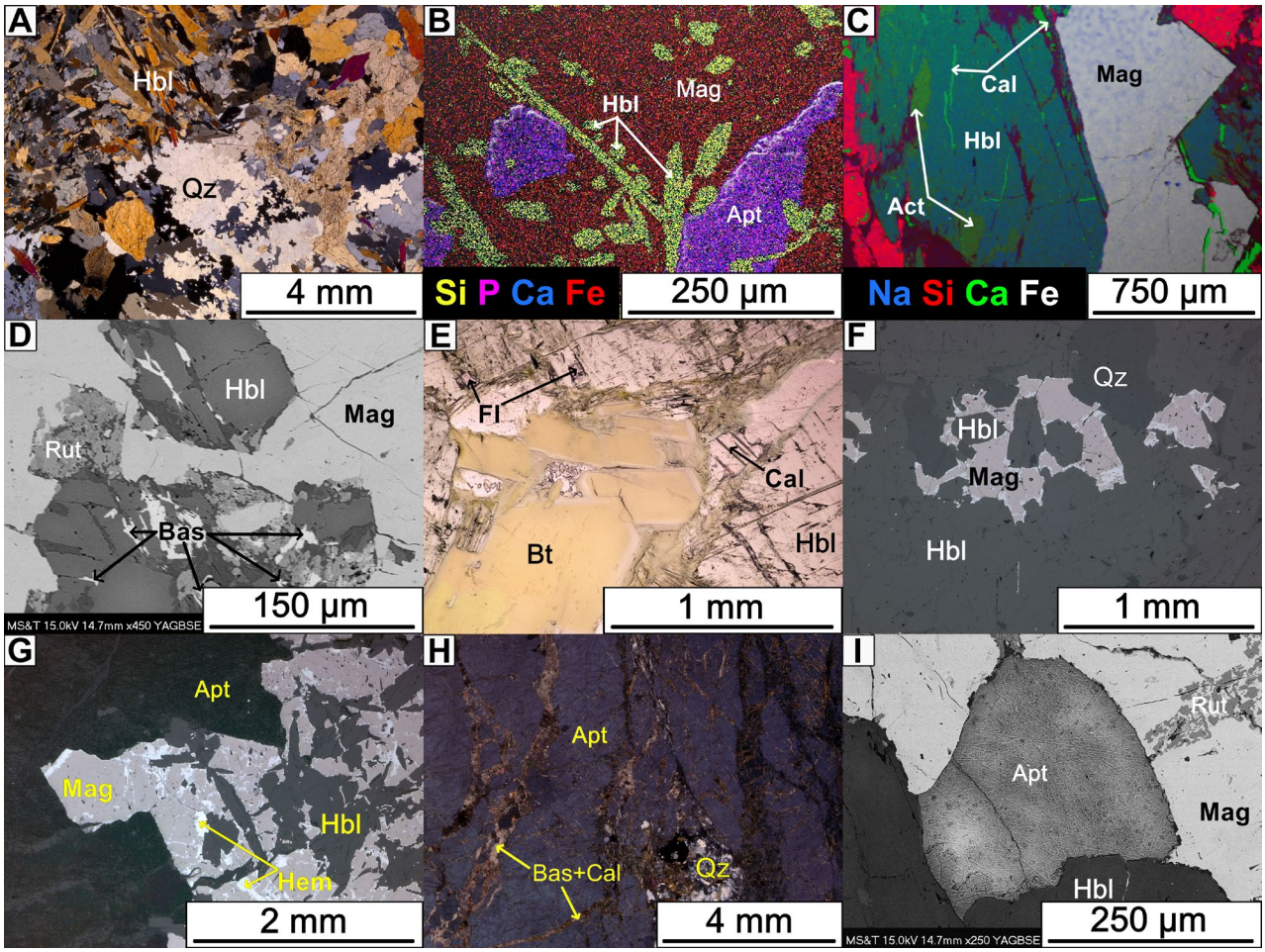

Fig. 5. Representative images of samples from the hornblende zone that show the sample mineralogy. (A) Transmitted-light image (cross-polarized) from sample 56W134TL6. (B) Composite energy dispersive x-ray spectroscopy (EDS) element distribution map from sample 57W122RL7. (C) Layered EDS element distribution map from sample 57W122TL9. (D) Backscattered electron (BSE) image from sample 57W122RL7. (E) Transmitted-light image (plane-polarized) from sample 57w122TL9. (F) Reflected-light image (plane-polarized) from sample 56W134RL6. (G) Reflected light image (plane-polarized) from sample 57W122RL5. (H) Transmitted light image (cross-polarized) from sample 56W134TL4. (I) BSE image from sample 57W122RL7. Abbreviations: Apt = apatite, Bas = bastnaesite, Bt = biotite, Cal = calcite, Fl = fluorite, Hbl = hornblende, Mag = magnetite, Qz = quartz, Rut = rutile.

cemented by martitic hematite, with pseudomorphs following magnetite in quartz-, dolomite-, and calcite-filled vugs. Quartz in this zone is drusy (Fig. 7D). Locally, zones of relict magnetism were observed using a magnet scribe, indicating that some of the magnetite had not been completely replaced, or possibly indicating the presence of maghemite. Martitic hematite decreases in abundance from 80 modal % near the Precambrian subcrop to 5 modal % at depths exceeding –200 m MSL. While hematite still occurs below –200 m (up to 50 modal %), it occurs predominantly as specular hematite and is generally less abundant than magnetite.

Red rhyolite unit: In areas where the hematite zones do not reach the Precambrian erosional surface, up to 40 m of heavily silicified extrusive red rhyolite is encountered between the Fe oxide zones and the Precambrian-Cambrian unconformity (Fig. 2). The silicified red rhyolite has very few phenocrysts, and where feldspar phenocrysts do occur, they are reddened and replaced by clays, sericite, or hematite. Groundmass in this unit is composed of crypto- to microcrystalline quartz and sericite. The red rhyolite zone also contains amygdules of quartz as well as infrequent millimeter-scale veins of hematite or quartz. The Precambrian-Cambrian unconformity surface is conglomeratic, with clasts of red rhyolite and hematite supported by a red-bedded lithic wacke matrix typical of the lowermost sections of the Cambrian Lamotte Sandstone (e.g., Houseknecht and Ethridge, 1978). The Precambrian subcrop at Kratz Spring is located below an additional 450 m of Cambrian to Ordovician sedimentary overburden.

Mafic dikes: Both the Kratz Spring North and South subdeposits are crosscut by a series of mafic to intermediate dikes and sills 1 to 10 m in thickness. These dikes and sills intersect all units apart from the Cambrian-Precambrian unconformity-associated conglomerate, indicating an emplacement age of anytime between 1.5 Ga and 500 Ma, i.e., bound by age of the 1.5 Ga St. Francois igneous province (Bickford et al., 2015) and the 500 Ma Lamotte Sandstone and basal conglomerate (Thompson et al., 2013). Textures observed in the mafic and intermediate dikes range from aphanitic to porphyritic

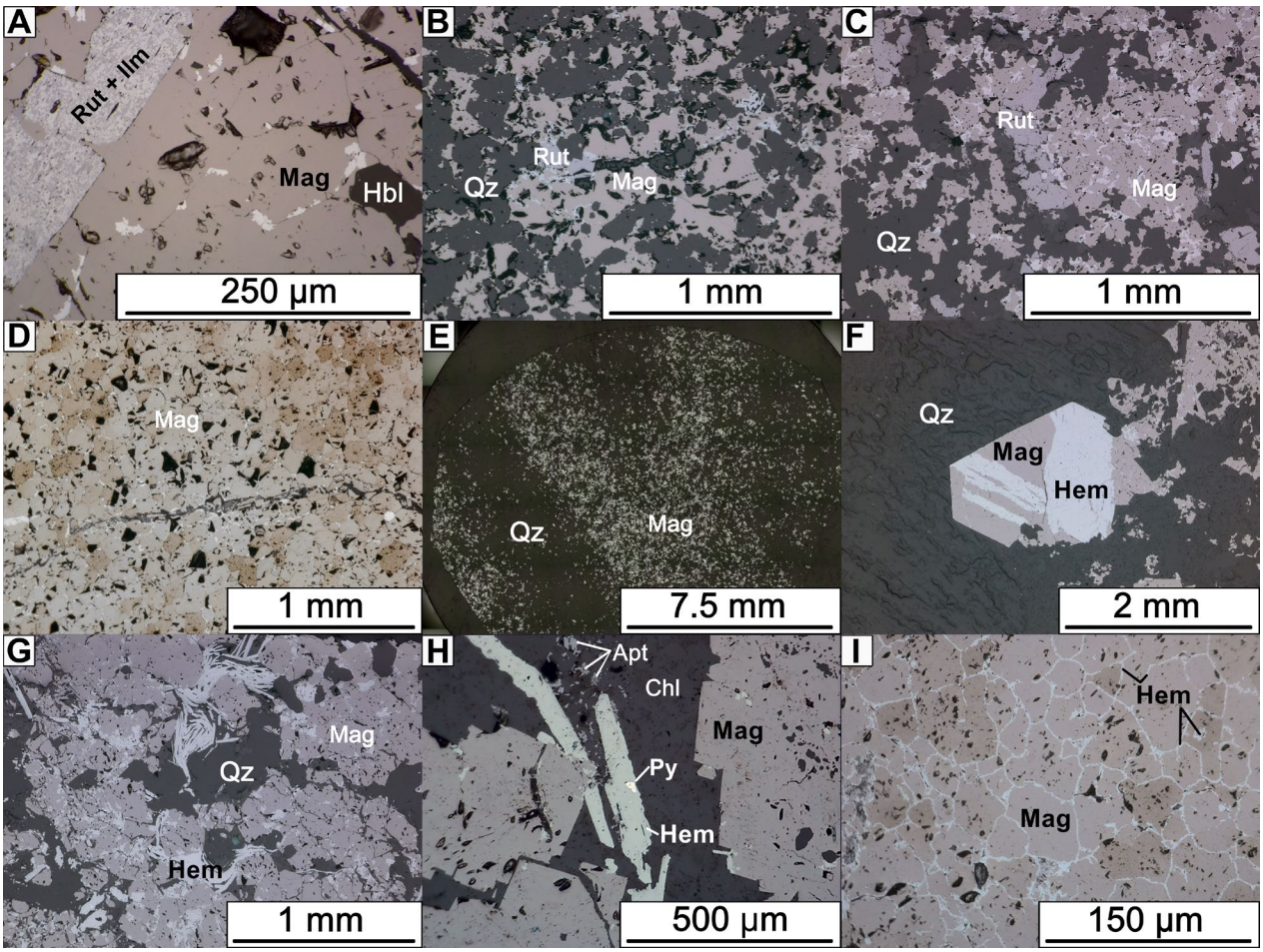

Fig. 6. Representative images of the magnetite zone from Kratz Spring that show the sample mineralogy. (A) Reflected-light image (plane-polarized) of Kratz Spring North sample 56w134RL1. (B) Reflected-light image (plane-polarized) from Kratz Spring South sample 58W47RL11. (C) Reflected-light image (plane-polarized) of Kratz Spring South sample 58W47RL8. (D) Reflected-light image (plane-polarized) from Kratz Spring North sample 57W122RL3. (E) Stitched reflected-light image (plane-polarized) in Kratz Spring South sample 58W47RL2. (F) Reflected-light image (plane-polarized) from Kratz Spring North sample 56W134RL2. (G) Reflected-light image (plain polarized) of Kratz Spring South sample 58W47RL6. (H) Reflected-light image (plane-polarized) from sample 58W47RL7. (I) Reflected-light image (plane-polarized) of sample 57W122RL1. Abbreviations: Apt = apatite, Chl = chlorite, Hbl = hornblende, Hem = hematite, Ilm = ilmenite, Mag = magnetite, Py = pyrite, Qz = quartz, Rut = rutile.

to fine-grained phaneritic. When discernable, phenocrysts are less than 2 mm in size and primarily composed of dark green-brown hornblende, orthopyroxene, and plagioclase (Fig. 8A). Hornblende and orthopyroxene frequently occur as inclusions in plagioclase (Fig. 8A). Round xenocrysts of quartz <2 mm in diameter were observed and display reaction rims 200 µm across (Fig. 8A). All mafic dikes are altered to some degree, with sericitic greening of plagioclase and replacement of mafic silicates with chlorite. Millimeter-scale epidote veins locally crosscut the mafic dikes and are similar in frequency and scale to those observed in the porphyry unit. Chromite was observed in a single sample from a mafic dike, occurring as 50-µm-diameter cores rimmed by magnetite (Fig. 8B). Some dikes close to the Precambrian-Lamotte contact contain micrometer-scale grains of chalcopyrite (Fig. 8B).

Salmon-colored aplite: The salmon-colored aplite is locally observed in approximately 20-m-thick magnetite-barren zones that interrupt massive beds of oxide mineralization in Kratz Spring South and is bleached to varying degrees (Fig. 2C). The aplite is an equigranular, aphanitic, leucogranitic, and highly silicic granitoid, with close to 75 modal % quartz. The quartz is both primary and secondary, with some weak granophyric intergrowths, but also quartz-sericite replacement of albite (Fig. 8C). Albite feldspar occurs between grains of quartz with a modal abundance of ~30% (Fig. 8C). Orthoclase feldspar is also present (approximately 20 modal %) and often associated with centimeter-thick veins composed of calcite, fluorite, specular hematite, quartz, and chlorite.

Mineral chemistry

Appendix Table A1 summarizes major and minor element chemistry for magnetite, hematite, and hornblende in Kratz Spring. Electron microprobe data for hematite and magnetite are shown in Appendix Table A1.2, and hornblende data are shown in Appendix Table A1.3 (all electron microprobe data are presented in oxide wt %). Individual LA-ICP-MS analyses

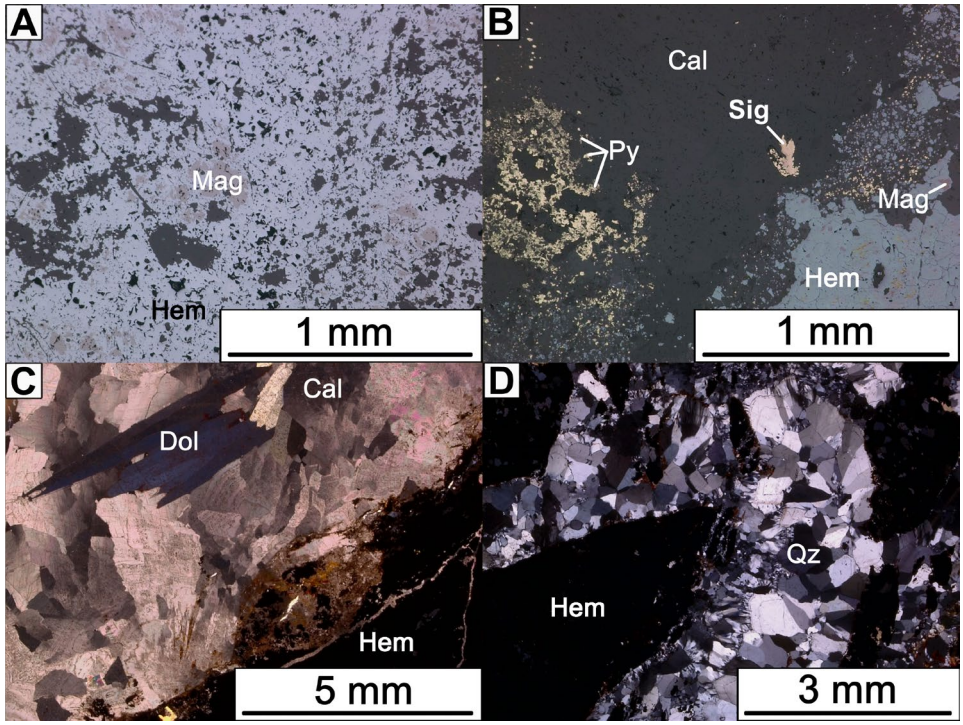

Fig. 7. Representative images from the hematite zone at Kratz Spring that show the sample mineralogy. (A) Reflected-light image (plane-polarized) in sample 56W131RL3. (B) Reflected-light image (plane-polarized) from sample 56W131RL2. (C) Transmitted-light image (cross-polarized) showing from sample 56W131TL2. (F) Transmitted-light image (cross-polarized) from sample 56W131TL1. Abbreviations: Cal = calcite, Dol = Dolomite, Hem = hematite, Mag = magnetite, Py = pyrite, Qz = quartz, Sig = siegenite ($CoNi_2S_4$).

are reported in ppm in Appendix Table A1.5 for magnetite and Table A1.6 for hematite. EMPA analyses show that hornblende at Kratz Spring North is edenite following the classification of Leake et al. (1997). The SiO_2 contents of Kratz Spring North edenite range from 43.2 to 52.8 wt % with MgO contents of 11.1 to 13.4 wt %. Concentrations of CaO are 5.7 to 7.7 wt %, whereas FeO contents range from 5.2 to 8.1 wt %. Aluminum contents are notably variable, ranging from 0.6 to 3.6 wt % Al_2O_3. All hornblende grains also contain notable amounts of Na (0.3–3.1 wt % Na_2O) and K (0.3–1.0 wt % K_2O), as well as minor amounts of Ti (0.04–0.3 wt % TiO_2).

The Fe content of magnetite ranges from 84 to 90 wt % FeO, measured by EPMA. All other minor and trace elements in magnetite and hematite were measured using LA-ICP-MS. Magnetite has Ti contents of 380 to 15,300 ppm and V contents of 400 to 1,050 ppm. It is noted that EPMA analyses of magnetite encounter wider ranges of TiO_2 contents, from below detection limits of 102 ppm to 6.97 wt % TiO_2. The implications of the observed high Ti variability in EPMA are discussed below. Specular hematite has FeO contents of 85 to 89 wt % and displays a strong variability in both Ti and V contents, with values between 3,200 and 7,000 ppm Ti and 930 and 1,020 ppm V. The Fe contents of martite range from 85 to 89 wt % FeO with 1,175 to 6,740 ppm Ti and 520 to 980 ppm V. Silica contents via EPMA are between 210 and 565 ppm Si in magnetite, between 390 and 1,589 ppm Si in specular hematite, and between 1,100 and 9,530 ppm Si in martite.

Figure 9 shows the magnetite and hematite minor and trace element chemistry normalized to the composition of the bulk continental crust and separated by depth, subdeposit (i.e., Kratz Spring North vs. South), and mineral texture (i.e., euhedral, disseminated, and massive). Lithophile trace elements that are incompatible into magnetite, such as Si, Ca, and Al, are strongly depleted in magnetite from both subdeposits (Fig. 9A). High field strength elements (HFSEs) are depleted in magnetite from both deposits, although it is noted that Zr, Nb, and Ta are generally more depleted than Hf. Magnetite from both deposits displays distinct positive Mo and Ge anomalies and negative Zr and Mg anomalies. Elements that are compatible in magnetite, such as Ti, Co, V, and Ni, i.e., with magnetite/intermediate melt partition coefficients greater than 1 (Dare et al., 2012), are relatively enriched when compared to the composition of the bulk continental crust. However, magnetite in both deposits is notably depleted in Cr despite Cr being the most compatible element into magnetite (Dare et al., 2012), resulting in an enrichment in Ni relative to Cr (high Ni/Cr ratio). Compatible elements show differences with respect to the subdeposit they were sampled from, with magnetite from Kratz Spring South containing less compatible trace elements than magnetite from Kratz Spring North, particularly Ti, Co, and V. Additionally, some incompatible granitophile elements, like Zr, Hf, Sc, and Sn, are distinctly enriched in Kratz Spring North magnetite when compared to Kratz Spring South magnetite. To a lesser extent, compatible element abundances in magnetite increase with depth in both deposits; this is especially evident in Mg and Zn in Kratz Spring North (Fig. 9A), where deeper samples (darker colors) have higher Mg contents than shallower samples (lighter colors).

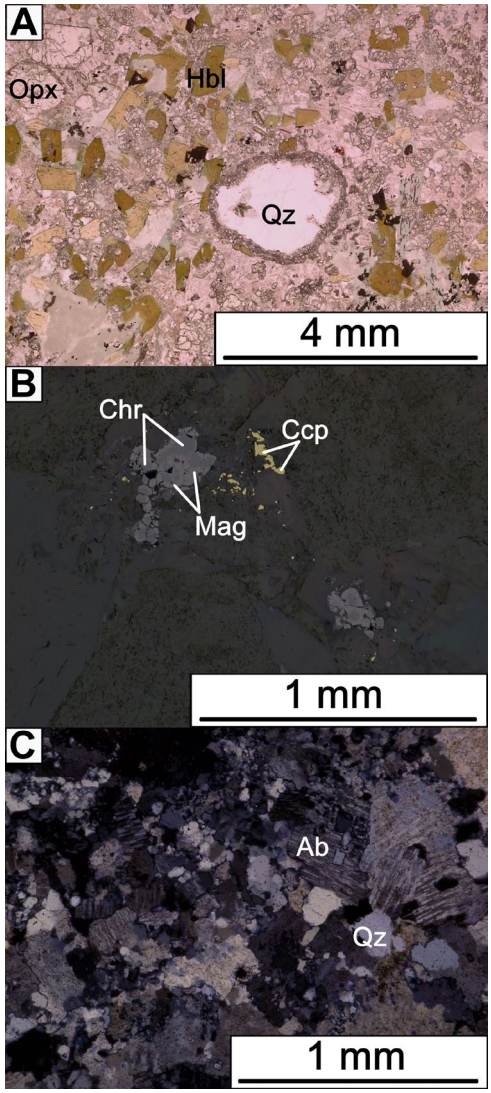

Fig. 8. Representative images of samples from mafic dikes in Kratz Spring North and salmon-colored aplite in Kratz Spring South showing mineralogy. (A) Transmitted-light image (plane-polarized) of mafic dike in sample 56w167TL1. (B) Reflected-light image (plane-polarized) sample 56W167TL1. (C) Transmitted-light image (cross-polarized) of the salmon-colored aplite from Kratz Spring South in sample 58w47. Abbreviations: Ab = albite, Ccp = chalcopyrite, Chr = chromite, Hbl = hornblende, Mag = magnetite, Opx = orthopyroxene, Qz = quartz.

Hematite analyzed from Kratz Spring North and South is predominantly similar to the trace element trends in magnetite other than Sn (Fig. 9B), which are discussed below. Therefore, hematite from Kratz Spring is depleted in Cr, lithophile elements (Si, Ca, Al, Mg), and HFSEs (Zr, Hf, Ta, Nb). The four different hematite types display distinct differences in their W, Sn, Mn, and Co contents. For example, specular hematite from the Kratz Spring North subdeposit has a trace element pattern distinct from specular hematite in Kratz Spring South and martitic hematite in both deposits. Specular hematite from Kratz Spring South differs from the other hematite species by more pronounced positive W and Sn anomalies and negative Mg anomalies when compared to the composition of the bulk continental crust (Fig. 9B). Martitic hematite and specular hematite from Kratz Spring South contain >100 ppm more W and Sn, 600 ppm less Mn, and 60 ppm less Co than hematite from Kratz Spring North.

As illustrated in Figure 10, hematite is characterized by REE contents 0.1 to 10 times that of C1 chondrite (McDonough and Sun, 1995). Specular hematite in both deposits and martitic hematite in Kratz Spring North are enriched in light (L)REEs compared to the C1 chondrite, with steep dips from La to Sm and a negative Eu anomaly. Specularite from Kratz Spring South shows a flat trend from Gd to Lu, while specularite and martite from Kratz Spring North show a positive slope from Gd to Lu (Fig. 10). Martitic hematite from Kratz Spring South contains a slight LREE depletion, a notably shallower Eu anomaly (when compared to specular hematite from both deposits and martite from Kratz Spring North), and a shallow negative slope from Gd to Lu. Hematite from both deposits is uniformly enriched in all REEs compared to magnetite, as magnetite contains REE contents generally below detection limits of 0.01 ppm.

Iron isotope composition

Stable iron isotope data of duplicate analyses of magnetite and hematite from the Kratz Spring deposit are reported in Appendix Table A2 and Figure 11 in standard-bracket-standard delta notation relative to IRMM-014. Three magnetite and two hematite samples from the Kratz Spring South subdeposit and one hematite and three magnetite samples from Kratz Spring North were analyzed. The iron isotope values from massive magnetite at Kratz Spring North were all negative, ranging from –2.14 to –0.06‰. Magnetite concentrates from greater depths at Kratz Spring North had δ^{56}Fe values closer to zero than those from shallower depths (cf. App. Tables A2, A4). Martitic hematite from Kratz Spring North was measured to have a δ^{56}Fe value of –1.94‰. Disseminated anhedral magnetite from the lower magnetite body at Kratz Spring South has δ^{56}Fe values from 0.14 to 0.20‰. The analysis of δ^{56}Fe values of specular hematite from the magnetite dominated zone in Kratz Spring South yielded a value of 0.06‰.

Bulk rock geochemistry

Figure 12 shows the C1 chondrite-normalized bulk rock compositions of rocks from Kratz Spring grouped by mineralization type, with the massive oxide mineralization field comprising hematite and magnetite lithologic zones, and the REE-enriched breccia field representing the phosphate-rich breccias and massive phosphate aggregates that can occur near the upper contact of the hornblende lithologic zone. The oxide mineralized zones show depletion across all REEs, with a curve pattern that is overall similar to the REE-enriched breccias, but without a negative Eu anomaly. The REE breccias show a steep slope from La to Gd with a flat, slightly concave slope from Gd to Lu. The breccias show a strong negative Eu anomaly and a positive Yb anomaly.

Discussion

The Kratz Spring deposit is one of several iron deposits in Missouri hosted in the Mesoproterozoic St. Francis Igneous Province. Compared to other deposits in the region, such as Pea Ridge (Ayuso et al., 2016; Childress et al., 2016; Day et al., 2016; Harlov et al., 2016; Hofstra et al., 2016; Neymark et al., 2016; Watts and Mercer, 2020), Boss (Seeger,

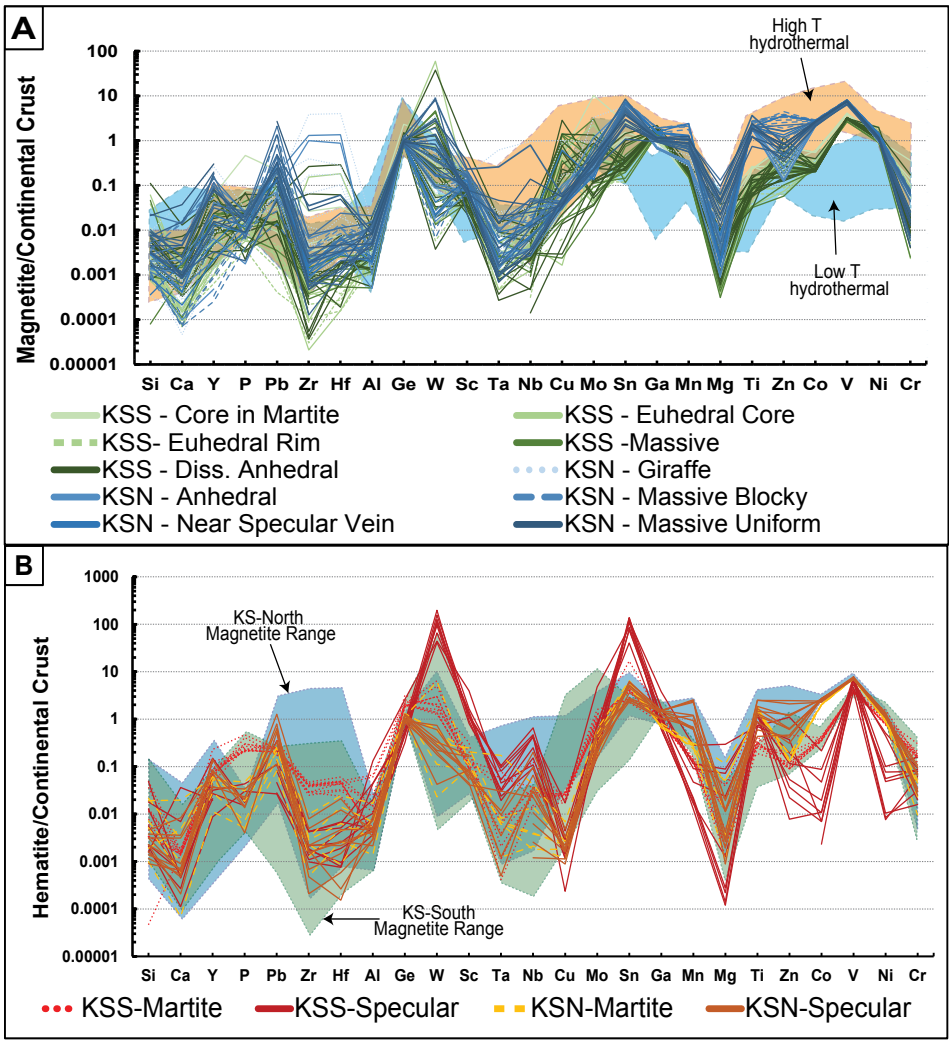

Fig. 9. Bulk continental crust-normalized trace element compositions of magnetite (A) and hematite with magnetite field (B) from Kratz Spring North (KSN) in blue and orange and Kratz Spring South (KSS) in green and red. Darker colors correspond with greater sample depths. Elements are in order of increasing compatibility into magnetite after Dare et al. (2014) with normalization values from Rudnick and Gao (2003). Zones for high (>~500°C)- and low (<~500°C)-T magnetite after Dare et al. (2014).

2003; Day et al., 2016; Mercer et al., 2020), Pilot Knob Magnetite, Pilot Knob Hematite, and Shephard Mountain (Nold et al., 2014; Childress et al., 2016; Tunnell et al., 2021, 2022), the Kratz Spring deposit is poorly characterized, and previous investigations were largely limited to core logging and bulk rock studies (Day et al., 2016). Here, we integrate new stratigraphic and petrographic descriptions with new mineral chemistry and iron isotope data to provide an improved description of the Kratz Spring deposit and propose a hydrothermal model for its genesis.

New constraints on the origin of the Kratz Spring deposit

Insight from deposit stratigraphy: Drill core studies show that the Kratz Spring deposit is divided into seven distinct lithologic units (Figs. 2, 3). Most of these units occur in both the Kratz Spring subdeposits; the only exceptions are post-ore mafic dikes, the hornblende unit that was only intersected at North, and the felsic dikes that were observed only at South.

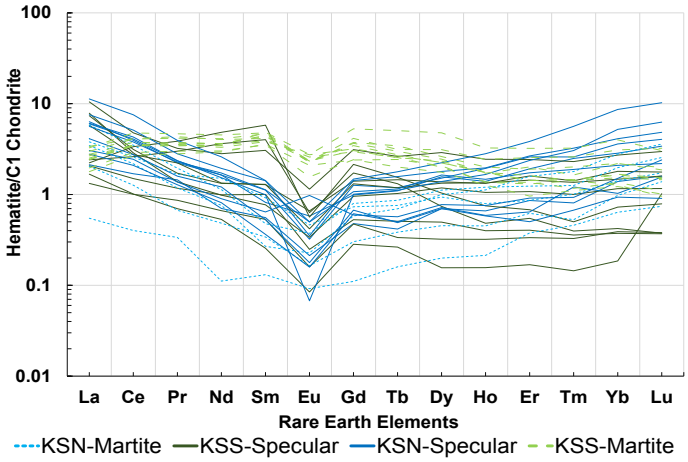

Fig. 10. C1 Chondrite (McDonough and Sun, 1995)-normalized rare earth element compositions of hematite from Kratz Spring South (KSS) in green and Kratz Spring North (KSN) in blue.

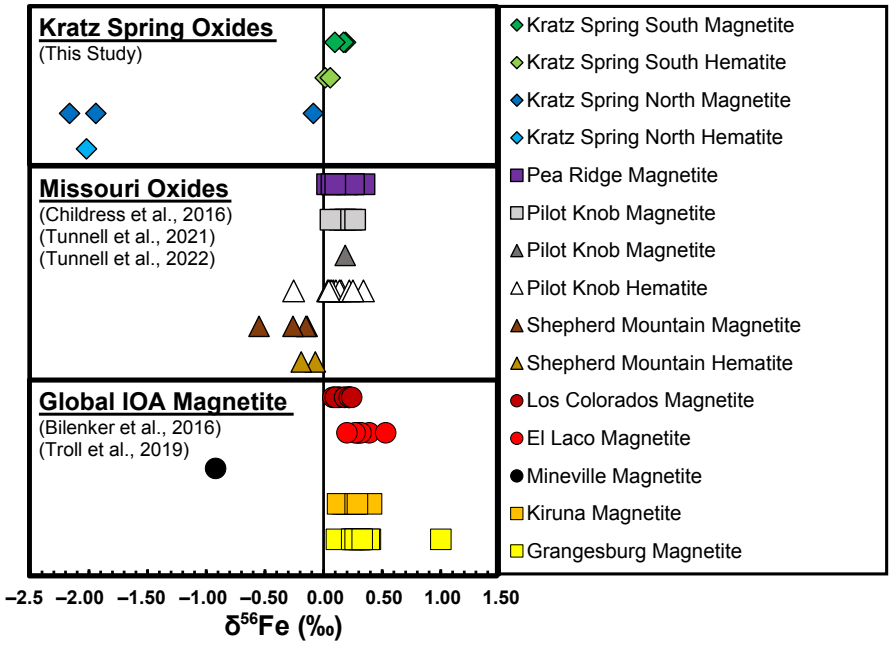

Fig. 11. Iron isotope data from Kratz Spring and various iron oxide-apatite (IOA) deposits presented in delta notation relative to IRRM-014. Isotope contents determined by multicollector-inductively coupled plasma-mass spectrometry (MC-ICP-MS) on mineral separates.

In both subdeposits, the Fe oxide mineralization is dominated by magnetite with lesser hematite. The magnetite bodies are concordant with the overall steeply dipping structure of the host rock units and appear to follow a dome or syncline structure at Kratz Spring North, where drill core data were available to develop a cross sectional deposit model (Fig. 2B). The structural relationships at Kratz Spring South are less well constrained because of a lack of drilling. However, because the host rock-ore contacts at Kratz Spring South exhibit steep angles relative to the drill core axes, it is likely that both subdeposits display a similarly steep dipping structure. It is noted that, while similar lithologic units and stratigraphic succession are encountered in both subdeposits, the elevation at which these units are encountered differ, i.e., Kratz Spring North was emplaced at least 200 m stratigraphically above Kratz Spring South based on the drill core studies presented here. Despite differences in the stratigraphic level, magnetite in both subdeposits transitions to martitic hematite-dominated mineralization at shallower depths (Figs. 2, 3).

Insight from magnetite chemistry and texture: Magnetite is the primary Fe carrier at Kratz Spring and formed during the main stage of mineralization in both subdeposits (Fig. 13). Consequently, understanding the formation conditions of magnetite provides insight into the primary mineralization mechanisms at Kratz Spring. Total trace element abundances in magnetite have been shown to increase with increasing formation temperature as cation distribution becomes more random due to lattice vibrations (Wu and Mason, 1981). Consequently, trace elements can partition into magnetite more readily at higher temperatures (Dare et al., 2014; Nadoll et al., 2014; Huang et al., 2019; Childress et al., 2020; Sievwright et al., 2020). As illustrated in Figure 8, magnetite from Kratz Spring North has a trace element pattern that follows the field of high-temperature (>500°C) hydrothermal magnetite (Dare et al., 2014) more closely than magnetite from Kratz Spring South, which mostly plots in the low-temperature hydrothermal field (Dare et al., 2014). The temperature difference between Kratz Spring North and South magnetite is further evident in Figure 14A, which shows that magnetite from North contains generally more Ti + V than magnetite from South. The separation of Kratz Spring North and South magnetite in this diagram is largely controlled by Ti contents, i.e., magnetite from North contains of ~3,100 to 15,300 ppm Ti (median = 8,175 ppm), whereas magnetite from South contains ~130 to 1,100 ppm Ti (median = 368 ppm; App. Table A1.5). Titanium and V are more compatible in magnetite at higher temperatures (Buddington and Lindsley, 1964). Therefore, the distinctly high Ti contents in magnetite from the Kratz Spring North subdeposit indicate that it formed at higher temperatures (most likely >500°C) when compared to the lower-Ti magnetite from Kratz Spring South.

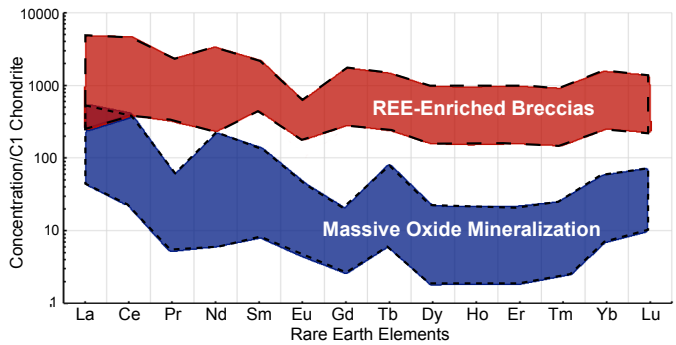

Fig. 12. Rare earth element (REE) plot for bulk rock data from Kratz Spring, including data from this study and United States Geological Survey data of Day et al. (2017) separated by lithology. Normalized to C1 Chondrite of McDonough and Sun (1995).

Textural evidence that supports a high-temperature origin of the magnetite mineralization at Kratz Spring North when compared to South includes magnetite's occurrence as vein/dike stockworks as well as breccia-hosted massive oxide mineralization solely at Kratz Spring North (Fig. 6A, D, I). The vein and breccia networks crosscut the host rock and include clasts derived from unaltered host rock and Mg-altered host rock units, thus implying that the Fe oxide mineralization was emplaced both after host rock formation and after the late Mg-rich edenite-forming alteration event. Veins and breccias like those observed at Kratz Spring North have been shown to reflect brittle fracturing of host rock upon outgassing of depressurized high-temperature melts or hydrothermal fluids upon ascent (Sillitoe, 1985).

In contrast to Kratz Spring North magnetite, lower Ti and V contents in magnetite from Kratz Spring South suggest that magnetite likely formed at temperatures near 300°C, following the Ti + V content methods of Nadoll et al. (2014) and Simon et al. (2018). Textural evidence further supports a lower-temperature formation of magnetite at Kratz Spring South, as magnetite displays disseminated to semimassive textures, with magnetite often occurring between grains of quartz (Fig. 6B, G). Such a texture, and the absence of evidence for oxide-associated brittle fracturing as in Kratz Spring North, likely reflects an in situ replacement of host rocks by oxides upon pervasive fluid infiltration (Nold et al., 2014; Tunnell et al., 2021). Fluid infiltration occurring along preexisting fabric within host rocks, e.g., flow banding, can explain the schlieren-like textures in Figures 3F and 6E that are solely observed in the Kratz Spring South deposit.

In addition to formation temperature, postformation events also can affect the mineral chemistry and texture of magnetite. Wen et al. (2017) demonstrated that, under some circumstances, reequilibration with hydrothermal fluids can increase Fe contents in magnetite, while its total trace element abundances decrease, resulting in apparent hydrothermal signatures of magmatic magnetite. Reequilibrated igneous magnetite can be distinguished from hydrothermal magnetite by plotting its degree of reequilibration (represented by Fe content; cf. Wen et al., 2017) against the V/Ti ratio. This approach is illustrated in Figure 14B, wherein the V/Ti ratio remains relatively constant as a function of reequilibration, creating a line of data points spreading between the magmatic and hydrothermal fields. Magnetite from Kratz Spring North, which displays mostly lower V/Ti ratios (0.08–0.3) with variable Fe contents (65–72 wt %), consequently plots along a linear trend between the hydrothermal and igneous magnetite field commonly associated with reequilibration of magnetite (Fig. 14B). When plotted against Kratz Spring South and other iron ore deposits in southeast Missouri, such as Pea Ridge (Huang et al., 2019), Pilot Knob, and Shepherd Mountain (Tunnell et al., 2022), notably, Kratz Spring North is the only deposit to have a single magnetite analysis that plots inside the magmatic field of Figure 14B. Further geochemical evidence for reequilibration of magnetite at Kratz Spring North includes grain-scale Ti mobility. While Ti is less mobile than other elements during reequilibration, it is noted that Ti can exhibit grain-scale mobility in magnetite during reequilibration by exsolving into nanoscale inclusions of rutile and/or

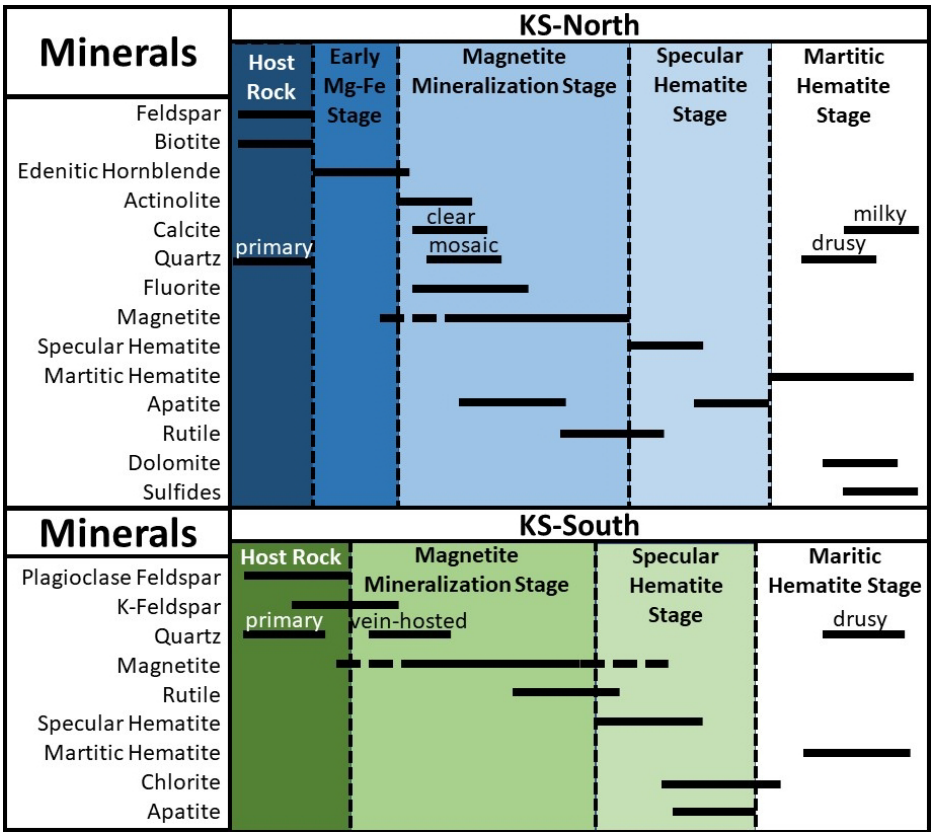

Fig. 13. Paragenetic relationships of different mineral phases observed at Kratz Spring, with each mineral on the Y axis and relative time on the X axis.

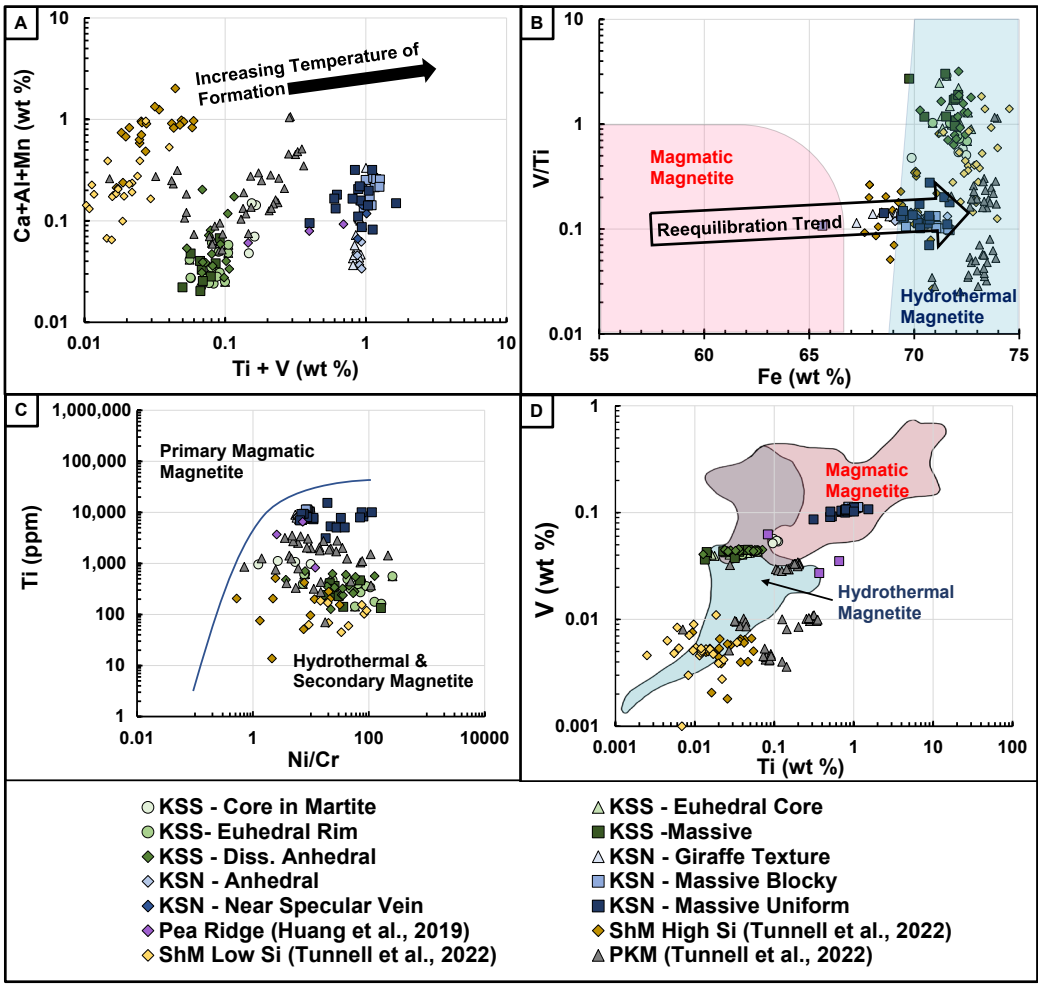

Fig. 14. Trace element discrimination diagrams for magnetite compositions determined by electron probe microanalysis (EPMA) and laser ablation-inductively coupled plasma-mass spectrometry (LA-ICP-MS) from Kratz Spring. Legend corresponds across all diagrams with all green samples from Kratz Spring South (KSS) and all blue samples from Kratz Spring North (KSN). Darker samples are from greater depths. (A) Scatter plot of Ca + Mn + Al against the Ti + V in wt %, all determined via LA-ICP-MS. (B) Scatter plot of Fe contents in wt % determined by EPMA against the V/Ti ratio determined by LA-ICP-MS. (C) Scatter plot of Ni/Cr ratio against Ti in ppm, all determined via LA-ICP-MS. (D) Scatter plot of V against Ti, both in wt %, determined via LA-ICP-MS. Plots developed by (A) Wen et al. (2017), (B) Huang et al. (2019), (C) Dare et al. (2014), (D) Knipping et al. (2015). Data from Kratz Spring supplemented by data from the Pea Ridge deposit (Huang et al., 2019), and the Shepherd Mountain (ShM) and Pilot Knob deposits (PKM) of Tunnell et al. (2022).

ilmenite that may be too small to be readily seen in SEM/BSE images (Knipping et al., 2015b; Wen et al., 2017; Simon et al., 2018). However, during this process, Ti will not depart the vicinity of the magnetite grain (Tan et al., 2015; Wen et al., 2017). The presence of nanoscale Ti-mineral inclusions in Kratz Spring North magnetite can potentially explain the greater variability in EPMA TiO_2 contents (102 ppm–6.97 wt %) when compared to the Ti contents measured by LA-ICP-MS (380–15,300 ppm Ti) because our microprobe analysis used a ~3-µm beam size, whereas our laser ablation spot size was 75 µm. Therefore, the EMPA data are more susceptible to submicrometer-scale inhomogeneities, which can result in high elemental variability as observed here for Ti (cf. Huang et al., 2019; Huang and Beaudoin, 2019). Notably, hydrothermal alteration was shown to not increase Ti or V contents in magnetite (Wen et al., 2017; Hou et al., 2020). In addition to the lines of geochemical evidence discussed above that support a reequilibration of magnetite, textural features in the vein- and breccia-hosted Kratz Spring North deposit that also support reequilibration of magnetite include grains that are equigranular, tightly intergrown, and display polygonal grain shapes with 120° triple junctions (Fig. 6I, D). Similar grain-scale features elsewhere were interpreted to reflect annealing of magnetite caused by reequilibration, for example in IOA deposits in the Chilean iron belt (Knipping et al., 2015b; Rodriguez-Mustafa et al., 2020; Palma et al., 2021), the Kiruna-Grangesberg district (Huang et al., 2019; Troll et al., 2019), and the Handang-Xingtai iron district (Wen et al., 2017). Annealing-associated reequilibration in these deposits was shown to be facilitated by magmatically exsolved fluids at temperatures between 300° and 750°C (cf. Hu et al., 2015; Wen et al., 2017).

Additional textural evidence for reequilibration at Kratz Spring North is observed in rutile. Magnetite and rutile gen-

erally share grain boundaries (Figs. 5I, 6A-C), indicating cocrystallization of both phases. However, rutile at Kratz Spring North solely occurs as mottled intergrowths (symplectites) or exsolution textures with magnetite and ilmenite (Figs. 5I, 6A), as opposed to Kratz Spring South, where rutile occurs as isolated subhedral grains (Fig. 6B-C). Ilmenite-rutile-magnetite symplectitic exsolutions such as the ones observed in Kratz Spring North (Fig. 6A) have been shown to reflect subsolidus hydrothermal reequilibration of ilmenite associated with magnetite at temperatures of at least 650°C (Tan et al., 2015; Wen et al., 2017; Tunnell et al., 2021). The high temperature range of rutile symplectites at Kratz Spring North indicates that the Fe oxide mineralization there must have formed from hydrothermal fluids at higher temperatures (650°–850°C), i.e., magmatically exsolved fluids, with subsequent modification by cooling of the hydrothermal fluids to 650°C that caused annealing and ilmenite-rutile-magnetite symplectites. Because the reequilibration of magnetite observed here occurs at temperatures between 300° and 750°C, the original crystallization temperature of Kratz Spring North magnetite must have been higher than 300°C, and potentially greater than 750°C (Wen et al., 2017). Furthermore, rutile symplectites observed ubiquitously at Kratz Spring North (Figs. 5I, 6A) form at temperatures greater than 650°C (Tan et al., 2015), narrowing T ranges of magnetite to greater than 650°C.

It is noted that the Ti contents in magnetite observed at Kratz Spring North (0.6–1.5 wt % Ti) preclude a formation temperature of greater than 850°C, based on the analysis of corresponding melt inclusions observed in other deposits (Nadoll et al., 2014; Knipping et al., 2019; Watts and Mercer, 2020). Therefore, a temperature range between 650° and 850°C is suggested for the formation of the Kratz Spring North magnetite. These observations are important because fluxed Fe-P melts have not been observed to remain liquid and immiscible below 1,000°C (Hou et al., 2018). As a consequence, the Ti contents of magnetite do not support Fe oxide formation from a fluxed oxide melt, but rather suggest either (1) magnetite precipitation from a 650° to 850°C, magmatically exsolved hydrothermal fluid or (2) formation from a water-rich melt or in-pluton orthomagmatic fluid followed by transport, concentration, and emplacement as a magnetite-fluid suspension. The emplacement mechanism we propose is similar to that suggested for other IOA deposits such as El Laco (Ovalle et al., 2018), Kirunavaara (Knipping et al., 2015a), and Pea Ridge (Watts and Mercer, 2020), but in contrast to these models, the origin of magnetite at Kratz Spring is entirely hydrothermal and not a continuum from igneous to hydrothermal, similar to the model of Tunnell et al. (2021).

A true hydrothermal signature is observed in magnetite from Kratz Spring South that plots within the hydrothermal and secondary magnetite field based on Fe contents (70–73 wt % Fe) and variable V/Ti ratios of 0.75 to 3.0. Consequently, the Ti, Fe, and V/Ti contents of magnetite support a low-temperature hydrothermal replacement model for Kratz Spring South, most likely at a temperature of approximately 300°C based on the Ti + V contents discussed above. A low-temperature hydrothermal origin with minor postmineralization reequilibration for Kratz Spring South magnetite is further supported by its consistently high Fe content when compared to other hydrothermal magnetite deposits in Missouri, including Pilot Knob and Shepherd Mountain (Fig. 14B; Tunnell et al., 2021, 2022). Textural evidence for Kratz Spring South magnetite being less affected by later reequilibration processes includes the notably larger range in magnetite grain sizes (i.e., <100 µm to >1 mm) when compared to Kratz Spring North, and lack of 120° triple junctions (Fig. 6G-H). As annealing causes grain sizes to become more uniform and polygonal in shape, the more variable grain sizes at Kratz Spring South suggest less pervasive annealing processes than at Kratz Spring North. In addition, the lack of rutile-ilmenite-magnetite symplectites, which are formed by reequilibration processes (Knipping et al., 2015b), confirms that annealing and/or reequilibration of magnetite at Kratz Spring South was negligible.

As discussed above, Kratz Spring South's magnetite chemistry and texture suggest that the mineralization formed during a lower-energy/lower-temperature hydrothermal replacement event when compared to the fracture-filling mineralization at Kratz Spring North. Based on these observations, we argue that Kratz Spring South magnetite mineralization formed at greater depths (i.e., based on current stratigraphic occurrence and replacement textures) but lower temperatures than the mineralization at Kratz Spring North. The higher hydrostatic pressure at Kratz Spring South, combined with the lower fluid temperatures, likely prevented the outgassing of depressurized hydrothermal fluids upon ascent. The lack of breccia-forming outgassing at Kratz Spring South resulted in the formation of pervasive replacement mineralization rather than the high-temperature, breccia/vein-hosted mineralization in the shallower Kratz Spring North deposit.

The proposed high-temperature (650°–850°C) hydrothermal origin of magnetite from Kratz Spring North and the lower-temperature (approx. 300°C) hydrothermal source for Kratz Spring South magnetite are also supported by the Ni/Cr and Ti composition of magnetite (Fig. 14C). Cr and Ni are the most compatible elements into magnetite and thus their abundance reflects well the composition of the magma/fluid from which magnetite crystallized (Dare et al., 2014). Cr is more immobile than Ni in hydrothermal fluids, thus resulting in a high Ni/Cr ratio for hydrothermal magnetite compared to that of igneous magnetite, where Cr is generally more rich than Ni due to its higher partition coefficient (Dare et al., 2014). Magnetite from both deposits at Kratz Spring plots clearly in the hydrothermal field, although magnetite from Kratz Spring North is characterized by notably higher Ti contents than most of the magnetite from Kratz Spring South (Fig. 14C), indicating a higher magnetite formation temperature (Dare et al., 2014; Nadoll et al., 2014). Exceptions to this generalization are the magnetite cores in some martitic hematite grains from Kratz Spring South that were affected by meteoric alteration. It is significant that magnetite from both subdeposits is characterized by notably low Cr contents (<15 ppm) resulting in the high Ni/Cr ratios shown in Figure 14C. Such low Cr contents preclude Fe oxide precipitation upon exsolution from a high-temperature (>950°C) Fe-Ca-P melt, as magnetite derived from such melts is generally characterized by Cr contents of >1,000 ppm (He et al., 2016) owing to Cr's affinity for Fe-Ca-P melts (Hou et al., 2018). This confirms that the low Cr and subsequent high Ni/Cr ratio of

magnetite are a hydrothermal signature, and that Ti content reflects different temperatures of the fluid.

Another tool that can be used to constrain magnetite formation mechanisms is illustrated in Figure 14D, which is based on observations derived from melt and fluid inclusion studies by Knipping et al. (2015b). Magnetite from Kratz Spring North plots within the field of magmatic magnetite owing to high Ti (3,119– 15,316 ppm) and V (864–1,136 ppm) concentrations (Fig. 14D), although their Ni/Cr ratios indicate that they are hydrothermal and not igneous. Conversely, most magnetite from Kratz Spring South has notably lower Ti (127–1,122 ppm) and V (364–568 ppm) contents and largely plots within the lower-temperature, fluid inclusion-bearing hydrothermal magnetite or the overlap between the magmatic and hydrothermal fields. Magnetites from other Missouri deposits including Pea Ridge (Huang et al., 2019), Pilot Knob, and Shepherd Mountain (Tunnell et al., 2022) are shown for comparison and plot primarily within and/or close to the hydrothermal magnetite field, most similar to Kratz Spring South magnetite (Fig. 14D).

Insight from hematite chemistry and texture: In contrast to the different modes of occurrence of magnetite and rutile in the Kratz Spring South and North deposits, specular and martitic hematite are notably similar in both subdeposits. Specular hematite occurs throughout both subdeposits and formed late in the petrogenetic sequence as inferred from its euhedral platy appearance exclusively interstitial to magnetite (Figs. 6G, 13). Martitic hematite is largely restricted to the uppermost portions of the deposits where it replaces magnetite (Figs. 6F, I, 7A). The replacement of magnetite by martitic hematite, but notably not by specular hematite, suggests that specular hematite formed during a distinct hydrothermal event at higher temperatures prior to the martitic hematite-forming event (Fig. 13). Specular hematite has been shown to form as a hydrothermal phase at temperatures between 150°C (Cabral and Rosière, 2013) and 462°C (Childress et al., 2020). In both deposits, specular hematite occurs before martitic hematite but after magnetite (Fig. 13), and so it could be argued that both subdeposits were affected by a late-stage (possibly the same), specular hematite-forming hydrothermal event at temperatures between 150° and 462°C. However, despite the similar platy appearance and premartite paragenesis of specular hematite in both subdeposits, several distinct differences exist in the mineral chemistry (Figs. 9B, 15). Most notably, specular hematite from Kratz Spring North displays elevated Mn concentrations (450–2,000 ppm Mn) when compared to specular hematite from Kratz Spring South (9–200 ppm Mn). The Mn contents likely reflect differences in redox and/or temperature conditions in the two subdeposits during specular hematite formation, as Mn can change to the 3+ valence from 2+ as a function of lowering temperatures and/or higher oxygen fugacity (Huebner and Sato, 1970; Sievwright et al., 2017). Trivalent Mn is more compatible in hematite than Mn^{2+} as it can replace Fe^{3+} (Huang et al., 2019). Consequently, the higher Mn concentrations at Kratz Spring North likely reflect formation of specular hematite from a more oxidizing and/or cooler fluid when compared to Kratz Spring South, possibly upon increased draw-down of meteoric water, as North is located at a stratigraphically higher level.

As shown in Fig. 15, both hematite groups from Kratz Spring South and North show a strong positive correlation between Mn and Co (Fig. 15B). While Mn contents in hematite can reflect both oxygen fugacity and temperature, Co incorporation into oxide minerals is largely controlled by the availability of sulfide minerals. Sulfides compete with oxides for Co when both phases are present in magmatic systems, lowering Co content in oxides (Duran et al., 2020). Although Co partitioning behavior in hydrothermal systems is less constrained,

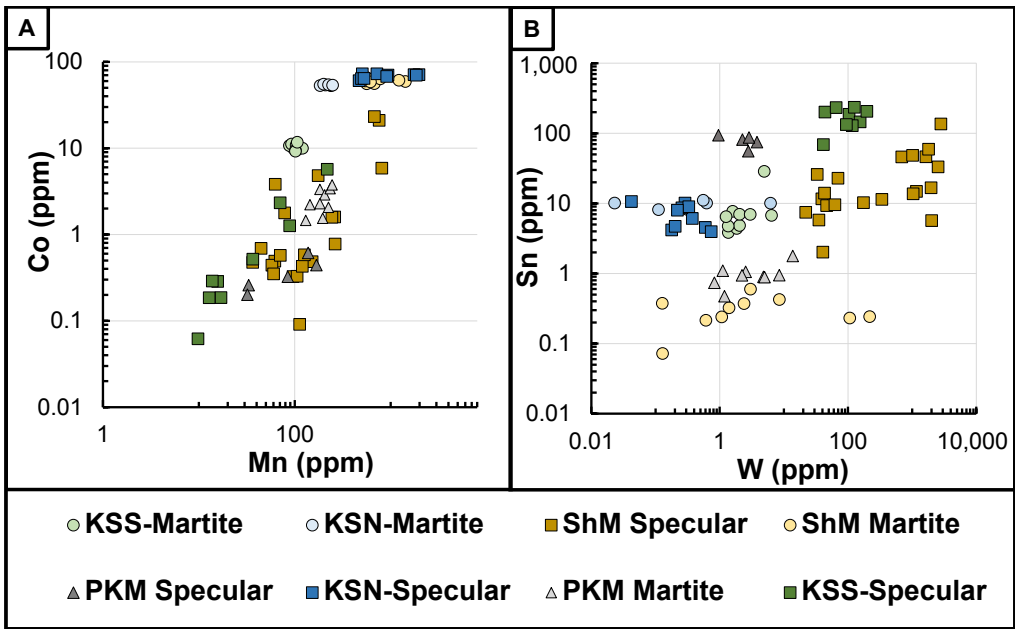

Fig. 15. Co vs. Mn (A) and Sn vs. W (B) diagrams in ppm. The key is the same for all diagrams, with green samples from Kratz Spring South (KSS) and blue samples from Kratz Spring North (KSN). All concentrations determined via laser ablation-inductively coupled plasma-mass spectrometry (LA-ICP-MS). Data from Kratz Spring supplemented by data from the Shepherd Mountain (ShM) and Pilot Knob deposits (PKM) of Tunnell et al. (2022).

several studies have observed lower Co contents (<10 ppm) in hydrothermal magnetite and hematite in sulfide-rich systems such as Cu-porphyries (Nadoll et al., 2014) and IOCG deposits (Courtney-Davies et al., 2019; Huang et al., 2019; Verdugo-Ihl et al., 2020) when compared to oxide-rich systems like IOA deposits (Huang et al., 2019). Based on the sulfide dependency, we argue that the higher Co contents in specular hematite at Kratz Spring North reflect hematite formation under sulfide-undersaturated conditions, petrographically supported by the absence of sulfides in the samples studied there. In contrast, the lower Co contents in specular hematite in Kratz Spring South suggest coprecipitating sulfide phases, supported by the presence of pyrite adjacent to, and as inclusions within, specular hematite in Kratz Spring South (Fig. 6H). Depletion of other chalcophile elements, including Zn and Ni, in Kratz Spring South specular hematite when compared to other hematite further supports that Kratz Spring South specular hematite formed from a more sulfide-rich hydrothermal fluid(s). Consequently, we argue that the correlation between Mn and Co suggests that Kratz Spring North specular hematite formed from a sulfide-poor, oxidizing, and/or cool meteoric fluid, whereas Kratz Spring South specular hematite formed from a more reduced and sulfide-rich hydrothermal fluid. It is noted that, while prevalent geochemical conditions during mineral precipitation may control Mn and Co contents in primary (i.e., specular) hematite, Mn and Co contents may also be inherited from the precursor mineral. Therefore, the Mn and Co contents in martitic hematite do not necessarily suggest its mineralization conditions but also may reflect the composition of the magnetite it replaced.

Specular and martitic hematites from Kratz Spring also display a positive correlation between W and Sn (Fig. 15C). An almost identical trend at similar concentrations was observed in hematite from the Wirrda Well and Acropolis IOCG prospects in the Gawler craton, Australia, with specular hematite locally containing >200 ppm Sn + W (Courtney-Davies et al., 2019). An Sn and W enrichment is also seen in hematite at the Shepherd Mountain deposit in Southeast Missouri, with hematite Sn + W contents of >200 ppm (Fig. 15; Tunnell et al., 2022). Additionally, Sn and W enrichment (>200 ppm Sn + W) is seen in bulk rock samples from several other Fe deposits in Southeast Missouri, including the Pea Ridge IOA deposit and the Boss IOCG deposit (Day et al., 2017). The Sn-W enrichment in some of Southeast Missouri's Fe oxide deposits is noteworthy as it contrasts with the granites and rhyolites elsewhere in the St. Francois Mountains that generally contain <30 ppm Sn + W (Day et al., 2017). Tin can behave as a compatible or incompatible element in granitic melts dependent on the local oxygen fugacity (Taylor and Wall, 1992; Blevin and Chappell., 1995). In oxidized melts, Sn is predominantly Sn^{4+}, becoming more compatible in oxide minerals, thus behaving as a compatible/lithophilic element (Taylor and Wall, 1992). In reduced melts, Sn is predominantly divalent and thus less compatible and more likely to enter hyperfractionated melts and orthomagmatic fluids (Taylor and Wall, 1992; Blevin and Chappell., 1995). Additionally, juvenile fluids rich in Cl have been shown to carry Sn and W, in some instances forming deposits of these elements (Wang et al., 2021). Consequently, the enrichment in Sn and W in Missouri IOA-IOCG deposits may suggest the orthomagmatic fluids that formed the deposits were derived from reduced melts and that Sn and W systematics are a potential exploration tool for IOA-IOCG systems in the region.

Chondrite-normalized REE patterns of martitic hematite and specular hematite from Kratz Spring North and specular hematite from Kratz Spring South are shown in Figure 10 and are characterized by an enrichment in LREEs and distinct negative Eu anomalies, thus mimicking the REE trends observed in bulk rock samples from the Fe oxide zones (Fig. 12). The most distinct difference between the REE composition of hematite (Fig. 10) and massive Fe oxide bulk rock data (Fig. 12) is an enrichment in the heavy rare earth elements (HREEs) in hematite. The enrichment does not necessarily reflect fluid chemistry, but more likely is the result of an increasing compatibility of the HREEs in hematite with increasing atomic number (Courtney-Davies et al., 2019; Xing et al., 2021). The REE contents of hematite are overall lower than the bulk rock REE contents, suggesting that REEs at Kratz Spring are primarily hosted by phases other than hematite, such as apatite and bastnaesite that occur throughout the deposit (Figs. 5D, H, 6H).

Specular hematite generally contains more REE mineral inclusions (such as bastnaesite) than magnetite in both subdeposits, whereas magnetite contains more inclusions of apatite, which contains less REEs than bastnaesite (Fig. 9), suggesting that the majority of the REEs were introduced by a late-stage hydrothermal fluid(s). In this scenario, the REE content of the fluid may have been scavenged from earlier-formed apatite elsewhere in the deposit, as evidenced by decomposition textures in apatite associated with bastnaesite (Fig. 5H). Scavenging of REEs during hematite formation is further suggested by apatite crystallizing before hematite (Fig. 13), and with magnetite as evidenced by intergrown textures (Fig. 5I) and inclusions. Alternatively, the similar REE patterns of hematite and the bulk rock samples could suggest that the hematite- and REE-mineral–forming fluid(s) had a similar chemistry or possibly were the same fluid. Hematite and apatite coprecipitation from the same fluid at Kratz Spring South is supported by the close spatial association of specular hematite and late-stage REE minerals throughout Kratz Spring (Fig. 6H), including shared grain boundaries with some apatite grains (Fig. 5G) and the observation that REE inclusions are more common in hematite than magnetite. The REE-rich fluid would have percolated through the deposit after magnetite crystallized.

At Kratz Spring North, martitic hematite has a mineral composition similar to the magnetite it replaced, displaying similar trends in the multielement diagram shown in Figure 9B. The similar concentrations of these elements in martitic hematite agree with other studies that showed that martite replacing magnetite inherits some of its trace element chemistry (e.g., Sidhu et al., 1981; Tunnell et al., 2022; Yin et al., 2022). It is noted, however, that martitic hematite at Kratz Spring North generally contains slightly lower overall trace element contents than the precursor magnetite, which indicates minor mobilization of these elements during martitization (Fig. 9B). Textural evidence for replacement of magnetite by martitic hematite in both deposits includes its replacement of magnetite with more intensity at shallower depths, particularly at Kratz Spring North, where massive hematite reaches and

is truncated by the Precambrian-Cambrian unconformity (Figs. 6I, 7A). In other magnetite-dominant Fe oxide deposits worldwide, martitic hematite forms from the replacement of magnetite; for example, upon interaction with oxidizing hydrothermal fluids up to 220°C (Zhao et al., 2019) or, alternatively, from alteration by meteoric water at temperatures as low as 61°C (Thorne et al., 2009). It is noted that martite can also form independent of changes in the local oxygen fugacity conditions, for example, in the presence of Ce at low temperature hydrothermal conditions (≤200°C) because Ce catalyzes the replacement reaction (Yin et al., 2022). Due to the well-defined formation temperature of martitic hematite (i.e., ≤200°C; Zhao et al., 2019; Xing et al., 2021; Yin et al., 2022) and its late paragenetic occurrence at Kratz Spring (Fig. 13), we argue that martitic hematite formed upon late-stage percolation by a Ce-rich hydrothermal or oxidized meteoric fluid with a temperature of ≤200°C. It is noted that the precise formation mechanism for martitic hematite could not be further constrained. For example, high Ce contents in bulk rock (Fig. 12) and martitic hematite (Fig. 10) suggest a redox-independent Ce-catalyzed replacement of magnetite by hematite (Yin et al., 2022). However, the stratigraphically constrained occurrence of martitic hematite close to the Precambrian-Cambrian unconformity instead suggests a meteoric origin for martitic hematite-forming fluids. Therefore, both a Ce-catalyzed and meteoric fluid-driven redox-controlled replacement of magnetite by martitic hematite are supported by the data presented. It is possible that either or both mechanisms of martitic hematite formation were responsible for formation of martitic hematite at Kratz Spring.

Insight from magnetite iron isotope chemistry: The iron isotope composition of magnetite can be used to determine iron sources. Igneous and magmatic-hydrothermal magnetite, i.e., iron sourced from magmas or associated exsolved fluids, has been shown to have δ^{56}Fe values between 0.00 and 0.85‰ (Jonsson et al., 2013; Weis, 2013; Bilenker et al., 2016; Troll et al., 2019; Tunnell et al., 2021). Conversely, lower-temperature hydrothermal systems (i.e., <200°C), as well as banded iron formations that form upon Fe oxide precipitation from surface waters, have strongly variable δ^{56}Fe values from –2.5 to 1.5‰ (Planavsky et al., 2012).

Magnetite δ^{56}Fe compositions from Kratz Spring South range from 0.1 to 0.2‰ (Fig. 11) and therefore fall within the range commonly associated with magma-sourced iron. Consequently, it can be argued that magnetite at Kratz Spring South either (1) crystallized directly from a magma, similar to models proposed for El Laco in Chile (Tornos et al., 2017; Hou et al., 2018), or (2) precipitated from a high-temperature hydrothermal fluid that exsolved from a deeper magma, as suggested for the Kirunavaara deposit in Sweden (Jonsson et al., 2013) and the Pilot Knob Magnetite deposit, U.S.A. (Tunnell et al., 2021). Due to the hydrothermal replacement textures seen in magnetite (Figs. 6B, E), and its low Ti contents (Fig. 14), we argue that magnetite at Kratz Spring South is more likely to have precipitated from a high-temperature hydrothermal/orthomagmatic fluid exsolved from a magma rather than direct oxide precipitation from a magma.

Magnetite from Kratz Spring North has δ^{56}Fe values between –2.17 and –0.09‰ (Fig. 11). Such negative values, and the large spread, generally preclude a solely igneous origin for magnetite (Jonsson et al., 2013; Weis, 2013; Bilenker et al., 2016; Troll et al., 2019; Tunnell et al., 2021, 2022) and rather suggest input of sedimentary iron or low-temperature fluids such as meteoric waters (Weis, 2013). It is worth noting that the δ^{56}Fe values in magnetite from Kratz Spring North decrease with decreasing depth from δ^{56}Fe = –0.09‰ at 576 m to δ^{56}Fe = –1.94‰ at 550 m and –2.17‰ at 535 m. The highly fractionated Fe isotope compositions at shallow depth likely reflect interaction with near-surface meteoric fluids.

For comparison, Figure 11 also shows δ^{56}Fe values of magnetite from other igneous-hosted iron deposits in Southeast Missouri, including magnetite from the Pea Ridge and Pilot Knob magnetite IOA deposits and the vein-type Shepherd Mountain deposit (Childress et al., 2016; Tunnell et al., 2021, 2022). Data from this study and previous studies have identified at least two provenances for Fe in the Fe oxide deposits of the St. Francois Terrane. Magnetites from Pea Ridge, Lower Pilot Knob, and Kratz Spring South have δ^{56}Fe values of between 0.01 and 0.4‰, indicating a juvenile magmatic source for Fe at these deposits. Magnetites from Shepherd Mountain and Kratz Spring North have similar negative δ^{56}Fe values of between –0.07 and –2.17‰, indicating a meteoric or sedimentary iron source. Varied sources for Fe terrane-wide could indicate fluid mixing during deposit formation or extensive reworking of Fe deposits by later sedimentary-sourced or meteoric fluids.

Insight from hematite iron isotope chemistry: Figure 11 shows δ^{56}Fe values of martitic hematite from Kratz Spring North and South and specular hematite from South alongside values from other Missouri deposits, including Shepherd Mountain (Tunnell et al., 2022) and upper Pilot Knob hematite (Tunnell et al., 2021). Compared to magnetite, studies on the iron isotope chemistry of hematite remain underrepresented in the literature; however, the limited published data suggest that Fe isotope behavior is similar between magnetite and hematite (Blanchard et al., 2009; Childress et al., 2020). Consequently, similar conclusions may be drawn between δ^{56}Fe values in hematite and magnetite; positive values that display narrow ranges may be indicative of magmatic Fe sources, whereas more variable (i.e., strongly negative to positive) values may represent a hydrothermal origin or possible sedimentary origin (Childress et al., 2020; Tunnell et al., 2021). Therefore, Fe isotope signatures of specular (primary) hematite can reveal fluid sources for late-stage fluid events. At Kratz Spring South, specular hematite had a δ^{56}Fe value of 0.06‰ and, consequently, we argue that this slightly positive value reflects derivation from a magma or a high-temperature, orthomagmatic hydrothermal fluid.

At Kratz Spring, the δ^{56}Fe values of martitic hematite generally mirror the values obtained for magnetite. At Kratz Spring South, martitic hematite has a δ^{56}Fe value of 0.01‰, while at Kratz Spring North, martitic hematite yielded a δ^{56}Fe value of –2.02‰ (Fig. 11). Magnetite, specular hematite, and martitic hematite at Kratz Spring South have similar δ^{56}Fe values of greater than 0 and less than 0.25‰. Similar to Kratz Spring South, the near-identical values of martitic hematite and magnetite at Kratz Spring North of approximately –2‰ support the experimental findings by Friedrich et al. (2019) that hematite replacement of magnetite does not necessarily alter its isotopic composition.

The distinctly low iron isotope value of –2.02‰ was measured in martitic hematite from a Kratz Spring North sample that represents the shallowest sample level (depth of 474 m). Analogous to the observations made for magnetite, this low isotope value likely reflects martitic hematite formation from a magnetite that had been previously reequilibrated by meteoric waters at shallow levels.

Insight from bulk rock chemistry: Bulk rock data from this study are used to constrain the lithology and tectonic origin of the Kratz Spring deposit and its host rocks. Figure 16A shows that the host rocks at both Kratz Spring subdeposits are predominantly rhyodacites/monzogranites based on Nb/Y and Zr/Ti ratios that are relatively immobile during alteration and therefore are less affected by later metamorphic and/or metasomatic alteration events (Winchester and Floyd, 1977; Day et al., 2016). The red rhyolite and basal porphyry units plot primarily in the upper portion of the rhyodacite/dacite fields, while the mafic dikes plot in the andesite and basaltic andesite fields. It is noted that Ti and Y are mobile in the Fe oxide zones at Kratz Spring, as Ti was redistributed during the emplacement of the Fe oxide bodies as shown by the occurrence of rutile and ilmenite associated with magnetite as well as Ti in magnetite itself. In addition, the alteration of ilmenite into rutile during reequilibration also mobilizes Ti (Rabbia et al., 2009; Tanis et al., 2016). The REE breccias and hornblende zones are enriched in yttrium hosted by phosphate and REE-carbonate minerals; as shown above, yttrium was likely transported by the same fluids that precipitated hematite. A similar mobility of Ti and REEs was observed in the nearby Pilot Knob hematite deposit (Fig. 1), where it was attributed to an F-rich, low-temperature (200°–250°C) oxidizing fluid that facilitated deposit genesis but did not significantly alter the host rocks (Tunnell et al., 2021). A similar F-rich fluid may have also infiltrated rocks in Kratz Spring, as evidenced by the presence of F-bearing phases like fluorite (Fig. 5E), bastnaesite (Figs. 5D, H), and fluorapatite (Figs. 5B, G-I).

Figure 16B shows that samples from the basal granite porphyry and the red rhyolite plot close to the junction of arc, ocean ridge, and within-plate granite tectonic regimes (Winchester and Floyd, 1977), suggesting a mixed source for the igneous rocks that host Kratz Spring and other regional IOA-IOCG deposits, as previously suggested by Day et al. (2016) and Watts and Mercer (2020). Previous studies have classified the host rocks of Kratz Spring as A-type granite/granitoid-derived volcanics (Day et al., 2016). As illustrated in Figure 17, host rocks of the Kratz Spring deposit plot within the A2-type granite field, indicating emplacement in a subduction-related extensional environment. Therefore, the bulk rock data support a model of back-arc extension or postorogenic extension for the St. Francois Igneous Province as recently proposed by Bickford et al. (2015), Watts and Mercer (2020), and Tunnell et al. (2021), as opposed to a true anorogenic continental rift or hotspot environment as suggested by Denison et al. (1984) and du Bray et al. (2021).

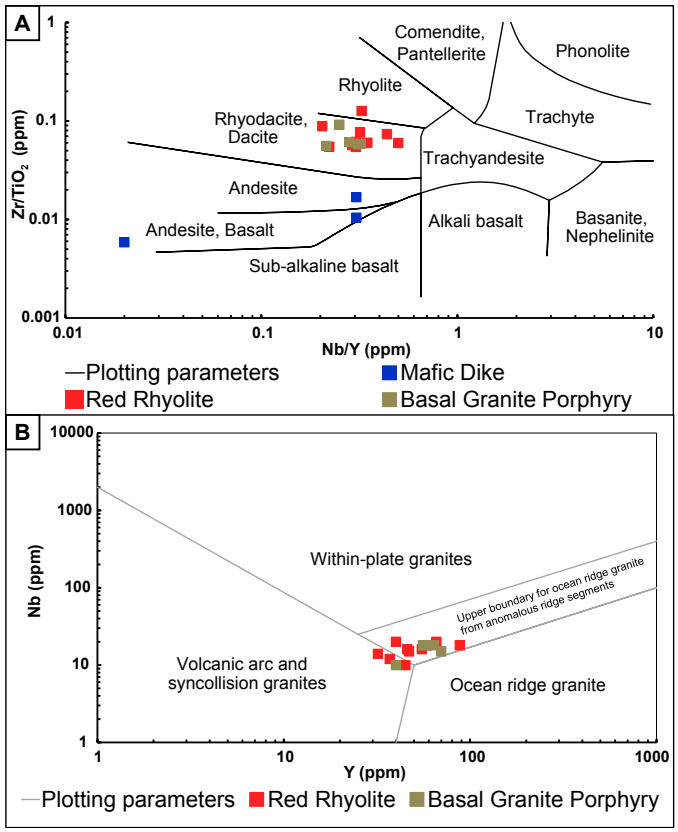

Fig. 16. Bulk rock data from Kratz Spring including United States Geological Survey data (Day et al., 2017) plotted on diagrams for protolith by Winchester and Floyd (1977), that plots Nb/Y ratios against Zr/Ti ratios (A) and tectonic environment by Pearce et al. (1984), that plot Y against Nb, both in ppm (B).

Models for the formation of the Kratz Spring deposit

Model for the formation of the Kratz Spring North subdeposit: Iron oxide mineralization at Kratz Spring formed at 1.455 Ga (Moscati and Neymark, 2021) as the result of at least three distinct mineralization events (Fig. 18). Before mineralization, percolation of host rocks by a high-temperature, Mg-rich fluid resulted in Mg-Ca-Fe alteration of the host rocks forming the hornblende zone. In the stratigraphically shallower Kratz Spring North deposit, the earliest oxide mineralization event is characterized by the formation of high-temperature hydrothermal magnetite at temperatures between 650° and 850°C, as shown by high Ti contents and high Ni/Cr ratios (Figs. 14A, D). The early magnetite was reequilibrated and annealed upon percolation by increasingly meteoric, lower-temperature fluid(s), causing annealing textures of magnetite (Fig. 6D, I), modification of the primary magnetite chemistry, most notably an increase in total Fe contents and decrease in alkali and alkali earth metal contents (Fig. 14B), and significant decrease of the δ^{56}Fe isotope composition of magnetite (Fig. 11). Additionally, the late-stage reequilibration of magnetite with the lower-T fluids likely triggered the replacement of ilmenite by rutile-magnetite symplectites, as these events occur at similar temperatures (Fig. 5D, I).

The reequilibration and annealing processes make it difficult to distinguish between high- and lower-T magnetite based on mineral chemistry because these later-stage processes overprinted the high-temperature chemistry of magnetite by increasing the Mg contents while decreasing the Fe. Texturally, annealing also caused any previous textures (such as rim-to-core transitions or fine-grained interstitial hydrothermal magnetite) to be replaced by equigranular magnetite. Consequently, while magnetite analyzed at Kratz Spring

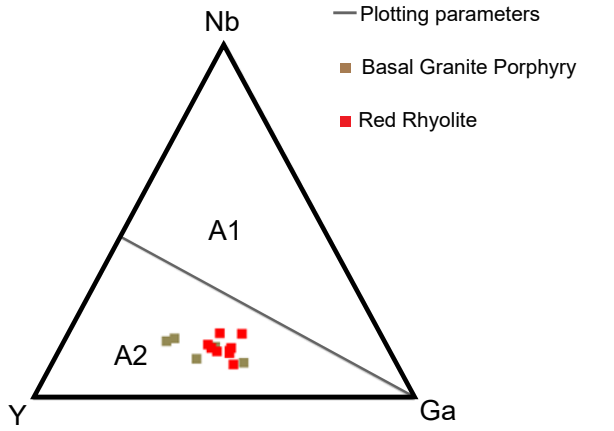

Fig. 17. Bulk rock data from Kratz Spring including United States Geological Survey data (Day et al., 2017) plotted on a ternary diagram that plots Y against Nb against Y, all in ppm. Plot developed by Eby (1992) to differentiate between A1- and A2-type granites.

North has somewhat uniform Ti, V, Ni, and Cr contents corresponding to crystallization from high-temperature hydrothermal fluids of magmatic origin, we cannot rule out accessory grains or rims of lower-temperature hydrothermal magnetite being present before reequilibration.

The proposed formation temperature of 650° to 850°C is notably higher than proposed formation temperatures in other regional IOA deposits (>500°C at Pilot Knob, Shephard Mountain, and Pea Ridge; Childress et al., 2016; Harlov et al., 2016; Hofstra et al., 2016; Johnson et al., 2016; Tunnell et al., 2021, 2022), and falls within emplacement temperatures of regional host granites and rhyolites (Watts and Mercer, 2020). While in situ hydrothermal replacement models have been proposed for other IOA deposits in southeast Missouri with lower Ti contents in magnetite and sub-500°C crystallization temperatures, the higher trace element contents in magnetite at Kratz Spring North indicate a higher temperature of magnetite formation more similar to preemplacement regional melts. Therefore, we propose a high-temperature mechanism for magnetite formation at Kratz Spring North, driven by orthomagmatic fluids generated by regional granitic magmas.

One such high-temperature IOA formation model is magnetite flotation, first proposed by Knipping et al. (2015a) and subsequently supported in experiments by Knipping et al. (2019). In the flotation model, supercritical fluid bubbles are generated upon depressurization of a volatile-rich, intermediate to granitic magma as it ascends higher in the crust. The bubbles nucleate onto magnetite due to magnetite's early crystallization and hydrophobic nature (Gualda and Ghiorso, 2007; Knipping et al., 2015a), allowing the resulting magnetite-bubble aggregates to overcome the high density of magnetite and ascend (i.e., "float"). It is noted that the magnetite flotation model requires multigenerational mixes of igneous and hydrothermal magnetite, which was not observed at Kratz Spring. However, the flotation model can be further refined by magnetite crystallizing from or in such supercritical fluid bubbles rather than simply adhering to them, as demonstrated by the experimental petrography work of Pleše et al. (2019). Magnetite crystallizing within the microenvironments in and around supercritical fluid bubbles is supported by the observation of high Ni/Cr ratios and low HFSE contents of magnetite from Kratz Spring North, as these elements avoid water-rich environments such as those expected in and around volatile-rich supercritical fluid bubbles in magmas. Additionally, since Figure 14D was derived by matching empirical observations of melt inclusions in magnetite to corresponding magnetite chemistry (Knipping et al., 2015b), the crystallization of magnetite from magmatic-exsolved hydrothermal fluids in a crystal mush environment can reconcile our observations with those of Knipping et al. (2015b).

During the fluid ascent, high-temperature hydrothermal magnetite is reequilibrated with the hydrothermal fluid bubbles as they cool, as well as any later fluid pulses. In such a scenario, magnetite ascends while cocrystallizing silicate minerals (feldspar, amphibole) sink within the magma chamber. A potential snapshot of this process can be seen in Figure 4A, where a zoned feldspar has magnetite grains trapped against it, implying that magnetite was being transported in a solid state. It is noted that similar mineralization processes, i.e., metal-rich mineral transport via attachment to bubbles, were recently attributed to the formation of some sulfide-mineralized and mantle-derived mafic-ultramafic rocks, such as at Norilsk-Talnakh in Russia (Barnes et al., 2019); Valmaggia in Italy (Locmelis et al., 2021); and several sulfide-bearing xenoliths in ultramafic rocks (Blanks et al., 2020), suggesting that supercritical volatile bubbles may play a more prominent role in ore genesis than previously thought.

In the flotation model, concentration of magnetite would be controlled by structural features along the periphery of the source , such as faults and cracks along caldera collapse structures that are frequently observed in the St. Francois Igneous Province (Kisvarsanyi and Kisvarsanyi, 1989; Day et al., 2016). Faults or cracks may act as preferred pathways for a magnetite-fluid suspension to migrate upward into solid country rock. Within such faults or cracks, magnetite-fluid suspensions can be trapped due to changes in fault geometry, as observed in other IOA deposits such as the Carmen and Fresia deposits in Chile (Palma et al., 2021) and the Pea Ridge deposit, U.S.A. (Day et al., 2016). By utilizing the magnetite-fluid suspension model in conjunction with existing transport and trap structures in the St. Francois Mountains terrane, a new model for the emplacement of Kratz Spring South and North was developed as illustrated in Figure 18. In this model, a felsic-intermediate (likely dacitic, cf. Tunnell et al., 2022) magma intruded beneath a series of normal faults along the edge of the 1.50 to 1.47 Ga Pea Ridge caldera structure (Kisvarsanyi and Kisvarsanyi, 1989; Day et al., 2016). The felsic-intermediate pluton exsolved fluids due to depressurization and/or a magma mixing event, similar to mixing events proposed at deposits in Chile, including Los Colorados, Carmen, and Fresia (Ovalle et al., 2018; Palma et al., 2021). Some of these fluid bubbles nucleated on the surface of magnetite, causing the magnetite-bubble pair to ascend in the magma chamber following the magnetite flotation model by Knipping et al. (2015a; 2019). The ascent of the fluid bubble-magnetite pairs was impeded by the top of the pluton, focusing it into overlying fault structures. Changes in fault geometry then acted as efficient magnetite traps as shown by the presence of magnetite mineralization in steeply dipping fault-controlled bodies.

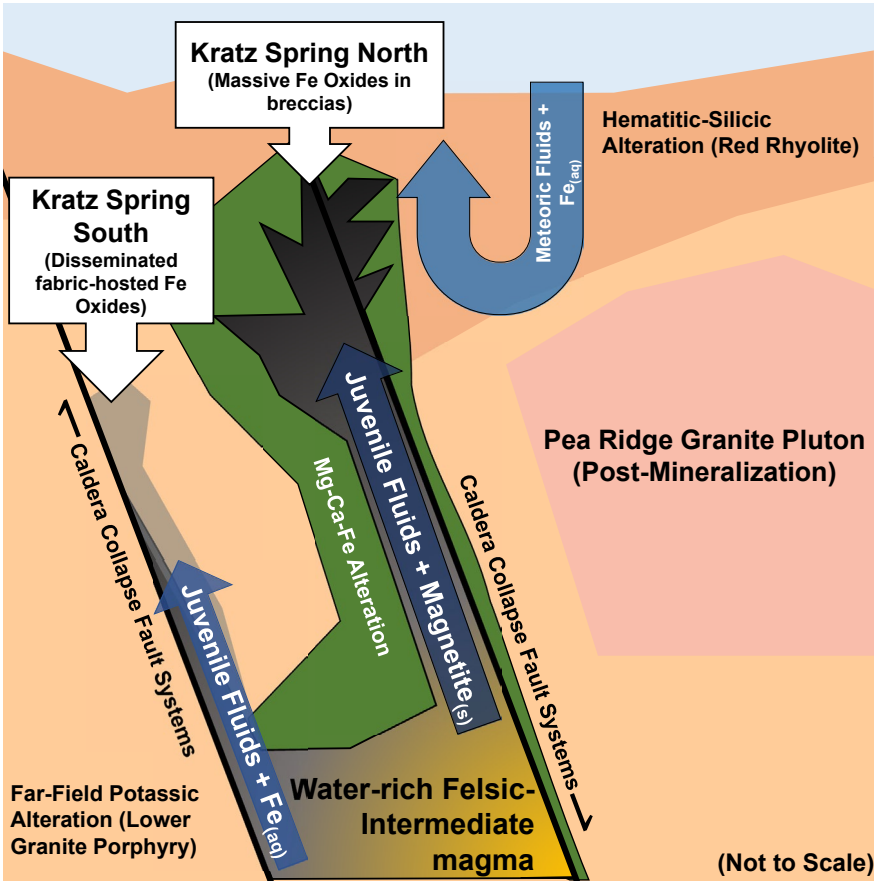

Fig. 18. Theoretical cross section of the formation processes in the larger Kratz Spring Deposit Complex. Regional caldera collapse fault systems and intermediate intrusive after Kisvarsanyi and Kisvarsanyi (1989), Seeger (2000), and Day et al. (2016).

Model for the formation of the Kratz Spring South subdeposit: In contrast to the high-temperature hydrothermal origin for magnetite at Kratz Spring North, magnetite at the stratigraphically deeper Kratz Spring South deposit formed from an Fe-rich hydrothermal fluid with a lower temperature of ~300°C, as evidenced by low total trace element contents, including Ti, in magnetite as discussed above (Fig. 14A). The iron isotope data presented in Figure 11 suggests that the hydrothermal fluid that formed Kratz Spring South magnetite was derived from a magma and had little to no meteoric input during (or after) mineralization. Rutile at Kratz Spring South formed contemporaneously with magnetite (Fig. 13), likely from the same hydrothermal fluid as discussed above. The magnetite-forming fluid at Kratz Spring South is characterized by a trace element pattern similar to that of magmatic fluids that formed Kratz Spring North magnetite (Fig. 9A), which may imply a genetic link between both deposits. In such a scenario, the deep magmatic event could have led to the emplacement of Fe oxide ore at different stratigraphic levels, with the hotter, more magmatic Kratz Spring North arm being emplaced closer to the surface than the cooler, hydrothermal Kratz Spring South arm. In this model, the Kratz Spring South deposit likely is a distal offshoot of a deeper magmatic plumbing system beneath Kratz Spring North, supported by its similar trace element magnetite chemistry to Kratz Spring North, its lower grades, smaller mineralized intercepts on the deposit scale, low-energy replacement petrographic textures, and lower-temperature mineral chemistry.

Low-temperature in situ hydrothermal replacement of host rocks by magnetite as proposed above for Kratz Spring North has been suggested for some time for several IOA deposits including the El Laco deposit in Chile (Dare et al., 2015) and the Pilot Knob (Nold et al., 2014; Tunnell et al., 2021, 2022) and Shephard Mountain deposits (Tunnell et al., 2022) in Missouri. In a replacement model for IOA deposit formation, high-T, reduced, and sulfur-poor fluids carried and deposited Fe while also replacing host rock minerals through dissolution-reprecipitation reactions (Corriveau et al., 2016). In IOA deposits attributed to in situ replacement, textural features used as evidence for the replacement model include along-fabric replacement of rock by magnetite, with magnetite surrounding chemically resistant phases such as quartz and zircon (Tunnell et al., 2021). Geochemical observations that also support a hydrothermal replacement model at other deposits include hydrothermal magnetite chemistry typified by low trace element contents and high Ni/Cr ratios (Nadoll et al., 2014; Dare et al., 2015). These petrographic and geochemical features are also comprehensively observed at Kratz Spring South, with magnetite from that deposit plotting close to magnetite from the hydrothermal Pilot Knob and Shepard Mountain deposits (Fig. 14). Based on the observations presented here, we argue that the Kratz Spring South deposit formed from in situ hydrothermal replacement of host rock along preexisting host rock fabric.

A comprehensive model for the Kratz Spring Deposit Complex: While the Kratz Spring North and South deposits display

different magnetite formation conditions, their proximity in time and space (Fig. 2a) and similar magnetite trace element chemistry (Fig. 9a) suggest a single genetic mechanism could link the two deposits. The flotation model of Knipping et al. (2015a, 2019), applied to our observations deposit-wide, suggests that fluid bubbles not attached to magnetite generally have a greater buoyancy owing to their lower density, and thus ascended faster than magnetite-bubble pairs. These fluid bubbles equilibrated with the felsic-intermediate melt and thus were Mg-Ca-Fe–rich, causing Mg-Ca-Fe wall alteration of host rock and the formation of the hornblende unit that predates the magnetite mineralization. Disseminated magnetite mineralization, most prominent in the more distal and cooler Kratz Spring South subdeposit, likely formed from precipitation of magnetite from Fe-saturated fluids upon cooling. Extensive disseminated magnetite mineralization likely also existed stratigraphically above the higher-temperature Kratz Spring North deposit but was likely eroded away during the formation of the Precambrian-Cambrian unconformity. The hydrothermal fluids that ascended along fault systems interacted with meteoric fluids near the surface, creating hydrothermal convection cells. The Kratz Spring North convection cell must have had a higher initial temperature owing to the higher temperature of the mineralization event when compared to Kratz Spring South. In contrast, the Kratz Spring North convection cell likely also had a stronger influx of meteoric fluids due to its higher emplacement level and/or more extensive degree of brecciation. The interaction of high-temperature fluids with the large amount of cooler meteoric fluids likely explains the isotopic and mineral chemical reequilibration in magnetite observed at Kratz Spring North. Conversely, at Kratz Spring South, deeper, initially cooler fluid cells were too deep to be affected by meteoric fluids, and instead remained magmatic-hydrothermal systems.

The Fe oxide mineralization at both Kratz Spring North and South shows evidence for late-stage overprints by cooler and more oxidizing fluids, which formed specular hematite veins that crosscut mineralization. At Kratz Spring North, the specular hematite-forming fluid was sulfide poor and oxidizing, diluted, and/or cooler and did not carry elements commonly associated with Cl-rich magmatic fluids (Wang et al., 2021), such as W and Sn. Hematite's chemistry at Kratz Spring North therefore suggests specular hematite-forming fluids were meteoric in origin, which is supported by hematite's strongly negative Fe isotope composition. Circulating hot meteoric-diluted fluids that reequilibrated magnetite also formed specular hematite at temperatures >350°C. While low-T meteoric fluids have not been shown to change magnetite's isotopic composition, hotter fluids can more destructively change magnetite's trace element and isotopic chemistry (Ye et al., 2020). At Kratz Spring South, specular hematite-forming fluids were more sulfide-rich, Cl-rich, and hotter and/or more reducing relative to the specular hematite-forming fluids at Kratz Spring North. Additionally, Kratz Spring South specular hematite-forming fluids carried elements often associated with magmatic fluids (W, Sn), and had an isotopic composition indicative of a juvenile source. Consequently, it is argued that the chemistry of specular hematite at Kratz Spring South indicates it was formed from a hydrothermal fluid of orthomagmatic origin. Following magnetite and specular hematite, martitic hematite formed in both deposits from a separate, much lower-temperature fluid event that was spatially limited to the uppermost portions of both deposits.

Conclusions

This study investigated and classified the two subdeposits of the larger Kratz Spring Deposit Complex, a ca. 1.455 Ga iron oxide-apatite deposit in southeast Missouri. Due to their proximity, previous studies assumed the Kratz Spring Deposit Complex to be one uniform deposit, but our findings show the following:

1. The Kratz Spring South and Kratz Spring North deposits are texturally unique at the deposit and mineral scale.
2. The Kratz Spring North deposit was formed through hydrothermal processes that emplaced a high-temperature magnetite, formed from orthomagmatic fluids at 650° to 850°C, that was subsequently reequilibrated by a heated, circulating meteoric fluid.
3. The Kratz Spring South deposit was formed through hydrothermal processes that emplaced lower-temperature hydrothermal magnetite which did not undergo measurable postemplacement reequilibration.
4. Specular hematite formed after magnetite in both deposits at low temperature (>350°C), albeit from different processes. At Kratz Spring North, specular hematite formed from fluids diluted by meteoric influx, while in Kratz Spring South, Sn-W–enriched hematite grains might have formed from a Cl-rich magma-derived hydrothermal fluid.
5. The Kratz Spring South and Kratz Spring North deposits are two expressions of the same magmatic-hydrothermal system related to granitic magmatism.

Acknowledgments

The authors thank the Missouri University of Science and Technology Radcliffe Scholarship, The Doe Run Company, and the National Science Foundation through CAREER Award#1944552 to M.L. for providing support for this project. We thank Larry Meinert for the editorial handling. The manuscript benefited greatly from critical reviews by two anonymous reviewers. The authors would also like to express gratitude to John Uhrie, Jim Palmer, Terry Peppers, and Chadley Hayes of the Doe Run Company for assisting with the sampling of drill core held at Doe Run Company facilities. Finally, the authors thank Audrie Lavoie at LabMaTer for running LA-ICP-MS analyses and Marc Choquette and Suzie Côté from Université Laval and Paul Carpenter from Washington University in St. Louis for running EPMA analyses.

REFERENCES

Aleinikoff, J.N., 2021, SHRIMP U-Pb geochronologic data for zircon and titanite from Mesoproterozoic rocks of the St. Francois Mountains terrane, southeast Missouri, U.S.A.: United States Geological Survey Data Release, doi: 10.5066/P95Q3QC4.

Ayuso, R.A., Slack, J.F., Day, W.C., and McCafferty, A.E., 2016, Geochemistry, Nd-Pb isotopes, and Pb-Pb ages of the Mesoproterozoic Pea Ridge iron oxide-apatite–rare earth element deposit, southeast Missouri: Economic Geology, v. 111, p. 1935–1962, doi:10.2113/econgeo.111.8.1935.

Barnes, S.J., Le Vaillant, M., Godel, B., and Lesher, C.M., 2019, Droplets and bubbles: Solidification of sulphide-rich vapour-saturated orthocumulates in

the Norilsk-Talnakh Ni-Cu-PGE ore-bearing intrusions: Journal of Petrology, v. 60, p. 269–300, doi:10.1093/petrology/egy114.

Barnes, S.-J., Maier, W., and Ashwal, L.D., 2004, Platinum-group element distribution in the Main Zone and Upper Zone of the Bushveld Complex, South Africa: Chemical Geology, v. 208, p. 293–317, doi: 10.1016/j.chemgeo.2004.04.018.

Barton, M.D., and Johnson, D.A., 1996, Evaporitic-source model for igneous-related Fe oxide–(REE-Cu-Au-U) mineralization: Geology, v. 24, p. 259–262, doi: 10.1130/0091-7613(1996)024<0259:ESMFIR>2.3.CO;2.

Bastrakov, E.N., Skirrow, R.G., and Davidson, G.J., 2007, Fluid evolution and origins of iron oxide Cu-Au prospects in the Olympic Dam District, Gawler craton, South Australia: Economic Geology, v. 102, p. 1415–1440, doi:10.2113/gsecongeo.102.8.1415.

Beard, B.L., Johnson, C.M., Von Damm, K.L., and Poulson, R.L., 2003, Iron isotope constraints on Fe cycling and mass balance in oxygenated Earth oceans: Geology, v. 31, p. 629–632, doi:10.1130/0091-7613(2003)031<0629:IICOFC>2.0.CO;2.

Best, M.G., Christiansen, E.H., de Silva, S., and Lipman, P.W., 2016, Slab-rollback ignimbrite flareups in the southern Great Basin and other Cenozoic American arcs: A distinct style of arc volcanism: Geosphere, v. 12, p. 1097–1135, doi:10.1130/GES01285.1.

Bickford, M.E., Van Schmus, W.R., Karlstrom, K.E., Mueller, P.A., and Kamenov, G.D., 2015, Mesoproterozoic-trans-Laurentian magmatism: A synthesis of continent-wide age distributions, new SIMS U-Pb ages, zircon saturation temperatures, and Hf and Nd isotopic compositions: Precambrian Research, v. 265, p. 286–312, doi:10.1016/j.precamres.2014.11.024.

Bilenker, L., Simon, A., Reich, M., Lundstrom, C., Gajos, N., Bindeman, I., Barra, F., and Munizaga, R., 2016, Fe-O stable isotope pairs elucidate a high-temperature origin of Chilean iron oxide-apatite deposits: Geochimica et Cosmochimica Acta, v. 177, doi: 10.1016/j.gca.2016.01.009.

Blanchard, M., Poitrasson, F., Méheut, M., Lazzeri, M., Mauri, F., and Balan, E., 2009, Iron isotope fractionation between pyrite (FeS_2), hematite (Fe_2O_3) and siderite ($FeCO_3$): A first-principles density functional theory study: Geochimica Et Cosmochimica Acta, v. 73, p. 6565–6578, doi: 10.1016/j.gca.2009.07.034.

Blanks, D.E., Holwell, D.A., Fiorentini, M.L., Moroni, M., Giuliani, A., Tassara, S., González-Jiménez, J.M., Boyce, A.J., and Ferrari, E., 2020, Fluxing of mantle carbon as a physical agent for metallogenic fertilization of the crust: Nature Communications, v. 11, p. 4342, doi: 10.1038/s41467-020-18157-6.

Blevin, P.L., and Chappell, B.W., 1995, Chemistry, origin, and evolution of mineralized granites in the Lachlan fold belt, Australia; the metallogeny of I- and S-type granites: Economic Geology, v. 90, p. 1604–1619, doi:10.2113/gsecongeo.90.6.1604.

du Bray, E.A., Aleinikoff, J.N., Day, W.C., Neymark, L.A., and Burgess, S.D., 2021, Petrology and geochronology of 1.48 to 1.45 Ga igneous rocks in the St. Francois Mountains terrane, southeast Missouri: U.S. Geological Survey Professional Paper, USGS Numbered Series 1866, doi:10.3133/pp1866.

Buddington, A.F., and Lindsley, D.H., 1964, Iron-titanium oxide minerals and synthetic equivalents: Journal of Petrology, v. 5, p. 310–357, doi:10.1093/petrology/5.2.310.

Cabral, A., and Rosière, C., 2013, The chemical composition of specular hematite from Tilkerode, Harz, Germany: Implications for the genesis of hydrothermal hematite and comparison with the Quadrilátero Ferrífero of Minas Gerais, Brazil: Mineralium Deposita, v. 48, doi: 10.1007/s00126-013-0459-2.

Campo-Rodríguez, Y.T., Schutesky, M.E., de Oliveira, C.G., and Whitehouse, M.J., 2022, Unveiling the polyphasic evolution of the Neoarchean IOCG Salobo deposit, Carajás Mineral Province, Brazil: Insights from magnetite trace elements and sulfur isotopes: Ore Geology Reviews, v. 140, article 104572, doi: 10.1016/j.oregeorev.2021.104572.

Childress, T.M., Simon, A.C., Day, W.C., Lundstrom, C.C., and Bindeman, I.N., 2016, Iron and oxygen isotope signatures of the Pea Ridge and Pilot Knob magnetite-apatite deposits, southeast Missouri, USA: Economic Geology, v. 111, p. 2033–2044, doi:10.2113/econgeo.111.8.2033.

Childress, T.M., Simon, A.C., Reich, M., Barra, F., Arce, M., Lundstrom, C.C., and Bindeman, I.N., 2020, Formation of the Mantoverde iron oxide-copper-gold (IOCG) deposit, Chile: Insights from Fe and O stable isotopes and comparisons with iron oxide-apatite (IOA) deposits: Mineralium Deposita, v. 55, p. 1489–1504, doi:10.1007/s00126-019-00936-x.

Corriveau, L., Montreuil, J.-F., and Potter, E.G., 2016, Alteration facies linkages among iron oxide copper-gold, iron oxide-apatite, and affiliated deposits in the Great Bear magmatic zone, Northwest Territories, Canada: Economic Geology, v. 111, p. 2045–2072, doi: 10.2113/econgeo.111.8.2045.

Courtney-Davies, L., Ciobanu, C.L., Verdugo-Ihl, M.R., Dmitrijeva, M., Cook, N.J., Ehrig, K., and Wade, B.P., 2019, Hematite geochemistry and geochronology resolve genetic and temporal links among iron-oxide copper gold systems, Olympic Dam district, South Australia: Precambrian Research, v. 335, article 105480, doi: 10.1016/j.precamres.2019.105480.

Dare, S.A.S., Barnes, S.-J., and Beaudoin, G., 2012, Variation in trace element content of magnetite crystallized from a fractionating sulfide liquid, Sudbury, Canada: Implications for provenance discrimination: Geochimica et Cosmochimica Acta, v. 88, p. 27–50, doi: 10.1016/j.gca.2012.04.032.

Dare, S.A.S., Barnes, S.-J., Beaudoin, G., Méric, J., Boutroy, E., and Potvin-Doucet, C., 2014, Trace elements in magnetite as petrogenetic indicators: Mineralium Deposita, v. 49, p. 785–796, doi: 10.1007/s00126-014-0529-0.

Dare, S.A.S., Barnes, S.-J., and Beaudoin, G., 2015, Did the massive magnetite "lava flows" of El Laco (Chile) form by magmatic or hydrothermal processes? New constraints from magnetite composition by LA-ICP-MS: Mineralium Deposita, v. 50, p. 607–617, doi: 10.1007/s00126-014-0560-1.

Day, W., Slack, J., Ayuso, R., and Seeger, C., 2016, Regional geologic and petrologic framework for iron oxide ± apatite ± rare earth element and iron oxide copper-gold deposits of the Mesoproterozoic St. Francois Mountains terrane, southeast Missouri, USA: Economic Geology, v. 111, p. 1825–1858, doi: 10.2113/econgeo.111.8.1825.

Day, W.C., Grannito, M., Ayuso, R.A., and Slack, J.F., 2017, Geochemical database for iron oxide-copper-cobalt-gold-rare earth element deposits of southeast Missouri: United States Geological Survey Data Release, doi: 10.5066/F7P26W67.

Del Real, I., Reich, M., Simon, A.C., Deditius, A., Barra, F., Rodríguez-Mustafa, M.A., Thompson, J.F.H., and Roberts, M.P., 2021, Formation of giant iron oxide-copper-gold deposits by superimposed, episodic hydrothermal pulses: Communications Earth & Environment, v. 2, p. 1–9, doi: 10.1038/s43247-021-00265-w.

Denison, R.E., Lidiak, E.G., Bickford, M.E., and Kisvarsanyi, E.B., 1984, Geology and geochronology of Precambrian rocks in the Central Interior region of the United States: United States Geological Survey, Professional Paper 1241C, doi: 10.3133/pp1241C.

Duran, C.J., Barnes, S.-J., Mansur, E.T., Dare, S.A.S., Bédard, L.P., and Sluzhenikin, S.F., 2020, Magnetite chemistry by LA-ICP-MS records sulfide fractional crystallization in massive nickel-copper-platinum group element ores from the Norilsk-Talnakh Mining District (Siberia, Russia): Implications for trace element partitioning into magnetite: Economic Geology, v. 115, p. 1245–1266, doi: 10.5382/econgeo.4742.

Eby, N., 1992, Chemical subdivision of the A-type granitoids: Petrogenetic and tectonic implications: Geology, v. 20, doi: 10.1130/0091-7613(1992)020<0641:CSOTAT>2.3.CO;2.

Ehrig, K., McPhie, J., and Kamenetsky, V., 2012, Geology and mineralogical zonation of the Olympic Dam iron oxide Cu-U-Au-Ag deposit, South Australia: Economic Geology, Special Publication no. 16, doi: 10.5382/SP.16.

Frierdich, A.J., Nebel, O., Beard, B.L., and Johnson, C.M., 2019, Iron isotope exchange and fractionation between hematite (α-Fe_2O_3) and aqueous Fe(II): A combined three-isotope and reversal-approach to equilibrium study: Geochimica et Cosmochimica Acta, v. 245, p. 207–221, doi: 10.1016/j.gca.2018.10.033.

Griffin, W.L., Powell, W.J., Pearson, N.J., and O'Reilly, S.Y., 2008, GLITTER: Data reduction software for laser ablation ICP-MS: Mineralogical Association of Canada, Short Course Series, v. 40, p. 308–311.

Gualda, G.A.R., and Ghiorso, M.S., 2007, Magnetite scavenging and the buoyancy of bubbles in magmas. Part 2: Energetics of crystal-bubble attachment in magmas: Contributions to Mineralogy and Petrology, v. 154, p. 479–490, doi: 10.1007/s00410-007-0206-8.

Harlov, D.E., Meighan, C.J., Kerr, I.D., and Samson, I.M., 2016, Mineralogy, chemistry, and fluid-aided evolution of the Pea Ridge Fe oxide-(Y + REE) deposit, southeast Missouri, USA: Economic Geology, v. 111, p. 1963–1984, doi: 10.2113/econgeo.111.8.1963.

He, H.-L., Yu, S.-Y., Song, X.-Y., Du, Z.-S., Dai, Z.-H., Zhou, T., and Xie, W., 2016, Origin of nelsonite and Fe-Ti oxides ore of the Damiao anorthosite complex, NE China: Evidence from trace element geochemistry of apatite, plagioclase, magnetite and ilmenite: Ore Geology Reviews, v. 79, p. 367–381, doi: 10.1016/j.oregeorev.2016.05.028.

Hofstra, A.H., Meighan, C.J., Song, X., Samson, I., Marsh, E.E., Lowers, H.A., Emsbo, P., and Hunt, A.G., 2016, Mineral thermometry and fluid inclusion studies of the Pea Ridge iron oxide-apatite–rare earth element deposit, Mesoproterozoic St. Francois Mountains terrane, southeast

Missouri, USA: Economic Geology, v. 111, p. 1985–2016, doi: 10.2113/econgeo.111.8.1985.

Hou, L., Liang, Q., and Wang, F., 2020, Mechanisms that control the adsorption-desorption behavior of phosphate on magnetite nanoparticles: The role of particle size and surface chemistry characteristics: RSC Advances, v. 10, p. 2378–2388, doi: 10.1039/C9RA08517C.

Hou, T., Charlier, B., Holtz, F., Veksler, I., Zhang, Z., Thomas, R., and Namur, O., 2018, Immiscible hydrous Fe-Ca-P melt and the origin of iron oxide-apatite ore deposits: Nature Communications, v. 9, p. 1415, doi: 10.1038/s41467-018-03761-4.

Houseknecht, D.W., and Ethridge, F.G., 1978, Depositional history of the Lamotte Sandstone of southeastern Missouri: Journal of Sedimentary Research, v. 48, p. 575–586, doi: 10.1306/212F74D7-2B24-11D7-8648000102C1865D.

Hu, H., Lentz, D., Li, J.-W., McCarron, T., Zhao, X.-F., and Hall, D., 2015, Reequilibration processes in magnetite from iron skarn deposits: Economic Geology, v. 110, p. 1–8, doi: 10.2113/econgeo.110.1.1.

Huang, X.-W., and Beaudoin, G., 2019, Textures and chemical compositions of magnetite from iron oxide copper-gold (IOCG) and Kiruna-Type iron oxide-apatite (IOA) deposits and their implications for ore genesis and magnetite classification schemes: Economic Geology, v. 114, p. 953–979, doi: 10.5382/econgeo.4651.

Huang, X.-W., Boutroy, É., Makvandi, S., Beaudoin, G., Corriveau, L., and De Toni, A.F., 2019, Trace element composition of iron oxides from IOCG and IOA deposits: Relationship to hydrothermal alteration and deposit subtypes: Mineralium Deposita, v. 54, p. 525–552, doi: 10.1007/s00126-018-0825-1.

Huebner, J.S., and Sato, M., 1970, The oxygen fugacity-temperature relationships of manganese oxide and nickel oxide buffers: American Mineralogist, v. 55, p. 934–952.

Jochum, K.P., Willbold, M., Raczek, I., Stoll, B., and Herwig, K., 2005, Chemical characterisation of the USGS reference glasses GSA-1G, GSC-1G, GSD-1G, GSE-1G, BCR-2G, BHVO-2G and BIR-1G using EPMA, ID-TIMS, ID-ICP-MS and LA-ICP-MS: Geostandards and Geoanalytical Research, v. 29, p. 285–302, doi: 10.1111/j.1751-908X.2005.tb00901.x.

Johnson, C.A., Day, W.C., and Rye, R.O., 2016, Oxygen, hydrogen, sulfur, and carbon isotopes in the Pea Ridge magnetite-apatite deposit, southeast Missouri, and sulfur isotope comparisons to other iron deposits in the region: Economic Geology, v. 111, p. 2017–2032, doi: 10.2113/econgeo.111.8.2017.

Jonsson, E., Troll, V.R., Högdahl, K., Harris, C., Weis, F., Nilsson, K.P., and Skelton, A., 2013, Magmatic origin of giant 'Kiruna-type' apatite-iron-oxide ores in Central Sweden: Scientific Reports, v. 3, p. 1644, doi: 10.1038/srep01644.

Kisvarsanyi, G., and Kisvarsanyi, E.B., 1989, Precambrian geology and ore deposits of the southeast Missouri Iron Metallogenic Province, in "Olympic Dam-Type" deposits and geology of middle Proterozoic rocks in the St. Francois Mountains terrane, Missouri: Society of Economic Geologists, Guidebook, v. 4

Kisvarsanyi, G., and Proctor, P.D., 1967, Trace-element content of magnetites and hematites, southeast Missouri metallogenetic province, U.S.A.: Economic Geology, v. 62, p. 449–471, doi: 10.2113/gsecongeo.62.4.449.

Knipping, J.L., Bilenker, L.D., Simon, A.C., Reich, M., Barra, F., Deditius, A.P., Lundstrom, C., Bindeman, I., and Munizaga, R., 2015a, Giant Kiruna-type deposits form by efficient flotation of magmatic magnetite suspensions: Geology, v. 43, p. 591–594, doi: 10.1130/G36650.1.

Knipping, J.L., Bilenker, L.D., Simon, A.C., Reich, M., Barra, F., Deditius, A.P., Wälle, M., Heinrich, C.A., Holtz, F., and Munizaga, R., 2015b, Trace elements in magnetite from massive iron oxide-apatite deposits indicate a combined formation by igneous and magmatic-hydrothermal processes: Geochimica et Cosmochimica Acta, v. 171, p. 15–38, doi: 10.1016/j.gca.2015.08.010.

Knipping, J.L., Webster, J.D., Simon, A.C., and Holtz, F., 2019, Accumulation of magnetite by flotation on bubbles during decompression of silicate magma: Scientific Reports, v. 9, p. 3852, doi: 10.1038/s41598-019-40376-1.

Leake, B., Woolley, A.R., Arps, C.E.S., Birch, W.D., Gilbert, M.C., et al., 1997, Nomenclature of amphiboles; Report of the Subcommittee on Amphiboles of the International Mineralogical Association, Commission on New Minerals and Mineral Names: American Mineralogist, v. 82, p. 1019–1037.

Locmelis, M., Moroni, M., Denyszyn, S.W., Webb, L.E., Fiorentini, M.L., Sessa, G., Caruso, S., Mathur, R., and Nanzad, B., 2021, On the formation of magmatic sulphide systems in the lower crust by long-lived mass transfer through the lithosphere: Insights from the Valmaggia pipe, Ivrea Verbano Zone, Italy: Terra Nova, v. 33, p. 137–149, doi: 10.1111/ter.12499.

Maréchal, C.N., Télouk, P., and Albarède, F., 1999, Precise analysis of copper and zinc isotopic compositions by plasma-source mass spectrometry: Chemical Geology, v. 156, p. 251–273, doi: 10.1016/S0009-2541(98)00191-0.

McCafferty, A.E., Phillips, J.D., and Driscoll, R.L., 2016, Magnetic and gravity gradiometry framework for Mesoproterozoic iron oxide-apatite and iron oxide-copper-gold deposits, southeast Missouri: Economic Geology, v. 111, p. 1859–1882, doi: 10.2113/econgeo.111.8.1859.

McDonough, W.F., and Sun, S.-s., 1995, The composition of the Earth: Chemical Geology, v. 120, p. 223–253, doi: 10.1016/0009-2541(94)00140-4.

McPhie, J., Kamenetsky, V.S., Chambefort, I., Ehrig, K., and Green, N., 2011, Origin of the supergiant Olympic Dam Cu-U-Au-Ag deposit, South Australia: Was a sedimentary basin involved?: Geology, v. 39, p. 795–798, doi: 10.1130/G31952.1.

Mercer, C.N., Watts, K.E., and Gross, J., 2020, Apatite trace element geochemistry and cathodoluminescent textures—A comparison between regional magmatism and the Pea Ridge IOAREE and Boss IOCG deposits, southeastern Missouri iron metallogenic province, USA: Ore Geology Reviews, v. 116, p. 103129, doi: 10.1016/j.oregeorev.2019.103129.

Moscati, R.J., and Neymark, L.A., 2021, In situ U-Pb dating of apatite and rutile from St. Francois Mountains IOA and IOCG deposits, southeast Missouri: United States Geological Survey Data Release, doi: 10.5066/P9EEV8E7.

Nadoll, P., Angerer, T., Mauk, J., French, D., and Walshe, J., 2014, The chemistry of hydrothermal magnetite: A review: Ore Geology Reviews, v. 61, p. 1–32, doi: 10.1016/j.oregeorev.2013.12.013.

Neymark, L.A., Holm-Denoma, C.S., Pietruszka, A.J., Aleinikoff, J.N., Fanning, C.M., Pillers, R.M., and Moscati, R.J., 2016, High spatial resolution U-Pb geochronology and Pb isotope geochemistry of magnetite-apatite ore from the Pea Ridge iron oxide-apatite deposit, St. Francois Mountains, southeast Missouri, USA: Economic Geology, v. 111, p. 1915–1933, doi: 10.2113/econgeo.111.8.1915.

Nold, J.L., Dudley, M.A., and Davidson, P., 2014, The southeast Missouri (USA) Proterozoic iron metallogenic province—Types of deposits and genetic relationships to magnetite-apatite and iron oxide-copper-gold deposits: Ore Geology Reviews, v. 57, p. 154–171, doi: 10.1016/j.oregeorev.2013.10.002.

Nuelle, L., Kisvarsanyi, E.B., Seeger, C., Day, W., and Sidder, G.B., 1991, Structural setting and control of the Pea Ridge magnetite deposit, Middle Proterozoic St. Francois terrane, Missouri: Abstracts and Programs of the Geological Society of America, v. 23, p. A292.

Oreskes, N., and Einaudi, M.T., 1992, Origin of hydrothermal fluids at Olympic Dam; preliminary results from fluid inclusions and stable isotopes: Economic Geology, v. 87, p. 64–90, doi: 10.2113/gsecongeo.87.1.64.

Ovalle, J.T., La Cruz, N.L., Reich, M., Barra, F., Simon, A.C., Konecke, B.A., Rodriguez-Mustafa, M.A., Deditius, A.P., Childress, T.M., and Morata, D., 2018, Formation of massive iron deposits linked to explosive volcanic eruptions: Scientific Reports, v. 8, article 14855, doi: 10.1038/s41598-018-33206-3.

Palma, G., Reich, M., Barra, F., Ovalle, J.T., del Real, I., and Simon, A.C., 2021, Thermal evolution of Andean iron oxide-apatite (IOA) deposits as revealed by magnetite thermometry: Scientific Reports, v. 11, article 18424, doi: 10.1038/s41598-021-97883-3.

Pearce, J.A., Harris, N.B.W., and Tindle, A.G., 1984, Trace element discrimination diagrams for the tectonic interpretation of granitic rocks: Journal of Petrology, v. 25, p. 956–983, doi: 10.1093/petrology/25.4.956.

Planavsky, N., Rouxel, O.J., Bekker, A., Hofmann, A., Little, C.T.S., and Lyons, T.W., 2012, Iron isotope composition of some Archean and Proterozoic iron formations: Geochimica et Cosmochimica Acta, v. 80, p. 158–169, doi: 10.1016/j.gca.2011.12.001.

Pleše, P., Higgins, M.D., Baker, D.R., Lanzafame, G., Kudrna Prašek, M., Mancini, L., and Rooyakkers, S.M., 2019, Production and detachment of oxide crystal shells on bubble walls during experimental vesiculation of andesitic magmas: Contributions to Mineralogy and Petrology, v. 174, p. 21, doi: 10.1007/s00410-019-1556-8.

Rabbia, O.M., Hernández, L.B., French, D.H., King, R.W., and Ayers, J.C., 2009, The El Teniente porphyry Cu-Mo deposit from a hydrothermal rutile perspective: Mineralium Deposita, v. 44, p. 849, doi: 10.1007/s00126-009-0252-4.

Rodriguez-Mustafa, M.A., Simon, A.C., del Real, I., Thompson, J.F.H., Bilenker, L.D., Barra, F., Bindeman, I., and Cadwell, D., 2020, A continuum from iron oxide copper-gold to iron oxide-apatite deposits: Evidence from Fe and O stable isotopes and trace element chemistry of magnetite: Economic Geology, v. 115, p. 1443–1459, doi: 10.5382/econgeo.4752.

Rudnick, R.L., and Gao, S., 2003, 3.01 - composition of the continental crust, *in* Holland, H.D., and Turekian, K.K., eds., Treatise on geochemistry: Oxford, Pergamon, p. 1–64, doi: 10.1016/B0-08-043751-6/03016-4.

Seeger, C.M., 2000, Southeast Missouri iron metallogenic province: characteristics and general chemistry, in Porter, T.M., ed., Hydrothermal iron oxide-copper-gold and related deposits: A global perspective, v. 1: Adelaide, PCG Publishing, p. 237–248.

Seeger, C.M., 2003, Lithology and alteration assemblages of the Boss iron-copper deposit, Iron and Dent Counties, southeast Missouri: Ph.D. thesis, Rolla, Missouri, University of Missouri-Rolla, 139 p.

Sidder, G.B., Day, W.C., Nuelle, L.M., Seeger, C.M., and Kisvarsanyi, E.B., 1993, Mineralogic and fluid inclusion studies of the Pea Ridge iron-rare-earth element deposit, southeast Missouri: United States Geological Survey, Bulletin 2039, p. 205–216.

Sidhu, P.S., Gilkes, R.J., and Posner, A.M., 1981, Oxidation and ejection of nickel and zinc from natural and synthetic magnetites: Soil Science Society of America Journal, v. 45, p. 641–644, doi: 10.2136/sssaj1981.03615995004500030041x.

Sievwright, R.H., Wilkinson, J.J., O'Neill, H.St.C., and Berry, A.J., 2017, Thermodynamic controls on element partitioning between titanomagnetite and andesitic-dacitic silicate melts: Contributions to Mineralogy and Petrology, v. 172, p. 62, doi: 10.1007/s00410-017-1385-6.

Sievwright, R.H., O'Neill, H.St.C., Tolley, J., Wilkinson, J.J., and Berry, A.J., 2020, Diffusion and partition coefficients of minor and trace elements in magnetite as a function of oxygen fugacity at 1150°C: Contributions to Mineralogy and Petrology, v. 175, p. 40, doi: 10.1007/s00410-020-01679-z.

Sillitoe, R.H., 1985, Ore-related breccias in volcanoplutonic arcs: Economic Geology, v. 80, p. 1467–1514, doi: 10.2113/gsecongeo.80.6.1467.

——2003, Iron oxide-copper-gold deposits: An Andean view: Mineralium Deposita, v. 38, p. 787–812.

Simon, A.C., Knipping, J., Reich, M., Barra, F., Deditius, A.P., Bilenker, L., and Childress, T., 2018, Kiruna-type iron oxide-apatite (IOA) and iron oxide copper-gold (IOCG) deposits form by a combination of igneous and magmatic-hydrothermal processes: Evidence from the Chilean iron belt: Society of Economic Geologists, Special Publication 21, p. 89–114.

Sims, P.K., Isvarsanyi, E.B.K., and Morey, G.B., 1987, Geology and metallogeny of Archean and Proterozoic basement terranes in the northern midcontinent, U.S.A.; An overview: United States Geological Survey, Numbered Series, no. 1815, doi: 10.3133/b1815.

Skirrow, R.G., 2022, Iron oxide copper-gold (IOCG) deposits—A review (part 1): Settings, mineralogy, ore geochemistry and classification: Ore Geology Reviews, v. 140, article 104569, doi: 10.1016/j.oregeorev.2021.104569.

Starkey, M.A., and Seeger, C.M., 2016, Mining and exploration history of the southeast Missouri Iron Metallogenic Province: Economic Geology, v. 111, p. 1815–1823, doi: 10.2113/econgeo.111.8.1815.

Storey, C.D., and Smith, M.P., 2017, Metal source and tectonic setting of iron oxide-copper-gold (IOCG) deposits: Evidence from an in situ Nd isotope study of titanite from Norrbotten, Sweden: Ore Geology Reviews, v. 81, p. 1287–1302, doi: 10.1016/j.oregeorev.2016.08.035.

Tan, W., Wang, C., He, H., Xing, C., Liang, X., and Dong, H., 2015, Magnetite-rutile symplectite derived from ilmenite-hematite solid solution in the Xinjie Fe-Ti oxide-bearing, mafic-ultramafic layered intrusion (SW China): American Mineralogist, v. 100, p. 2348–2351, doi: 10.2138/am-2015-5435.

Tanis, E.A., Simon, A., Zhang, Y., Chow, P., Xiao, Y., Hanchar, J.M., Tschauner, O., and Shen, G., 2016, Rutile solubility in NaF-NaCl-KCl–bearing aqueous fluids at 0.5–2.79 GPa and 250–650°C: Geochimica et Cosmochimica Acta, v. 177, p. 170–181, doi: 10.1016/j.gca.2016.01.003.

Taylor, J.R., and Wall, V.J., 1992, The behavior of tin in granitoid magmas: Economic Geology, v. 87, p. 403–420, doi: 10.2113/gsecongeo.87.2.403.

Thompson, T.L., Mulvany, P.S., Palmer, J.R., Miller, J.F., and Davis, J.G., 2013, Cambrian stratigraphic succession in Misssouri, *in* Paleozoic succession in Missouri Part 1 (revised) Cambrian System: Missouri Geological Survey, Report of Investigation 70, p. 25–56.

Thorne, W., Hagemann, S., Vennemann, T., and Oliver, N., 2009, Oxygen isotope compositions of iron oxides from high-grade BIF-hosted iron ore deposits of the Central Hamersley Province, Western Australia: Constraints on the evolution of hydrothermal fluids: Economic Geology, v. 104, p. 1019–1035, doi: 10.2113/econgeo.104.7.1019.

Tornos, F., Velasco, F., and Hanchar, J.M., 2017, The magmatic to magmatic-hydrothermal evolution of the El Laco deposit (Chile) and its implications for the fenesis of magnetite-apatite deposits: Economic Geology, v. 112, p. 1595–1628, doi: 10.5382/econgeo.2017.4523.

Troll, V.R., Weis, F.A., Jonsson, E., Andersson, U.B., Majidi, S.A., et al., 2019, Global Fe-O isotope correlation reveals magmatic origin of Kiruna-type apatite-iron-oxide ores: Nature Communications, v. 10, p. 1712, doi: 10.1038/s41467-019-09244-4.

Tunnell, B.N., Locmelis, M., Seeger, C., Mathur, R., Dunkl, I., Sullivan, B., and Lori, L., 2021, The Pilot Knob iron ore deposits in southeast Missouri, USA: A high-to-low temperature magmatic-hydrothermal continuum: Ore Geology Reviews, doi: 10.1016/j.oregeorev.2020.103973.

Tunnell, B.N., Locmelis, M., Seeger, C., Moroni, M., Dare, S., Mathur, R., and Sullivan, B., 2022, The Shepherd Mountain iron ore deposit in Southeast Missouri, USA—An extension of the Pilot Knob magmatic-hydrothermal ore system: Evidence from iron oxide chemistry: Ore Geology Reviews, v. 141, p. 104633, doi: 10.1016/j.oregeorev.2021.104633.

Verdugo-Ihl, M.R., Ciobanu, C.L., Cook, N.J., Ehrig, K., Slattery, A., and Courtney-Davies, L., 2020, Trace-element remobilisation from W-Sn-U-Pb zoned hematite: Nanoscale insights into a mineral geochronometer behaviour during interaction with fluids: Mineralogical Magazine, v. 84, p. 502–516, doi: 10.1180/mgm.2020.49.

Wang, T., She, J.-X., Yin, K., Wang, K., Zhang, Y., Lu, X., Liu, X., and Li, W., 2021, Sn(II) chloride speciation and equilibrium Sn isotope fractionation under hydrothermal conditions: A first principles study: Geochimica et Cosmochimica Acta, v. 300, p. 25–43, doi: 10.1016/j.gca.2021.02.023.

Watts, K.E., and Mercer, C.N., 2020, Zircon-hosted melt inclusion record of silicic magmatism in the Mesoproterozoic St. Francois Mountains terrane, Missouri: Origin of the Pea Ridge iron oxide-apatite-rare earth element deposit and implications for regional crustal pathways of mineralization: Geochimica et Cosmochimica Acta, v. 272, p. 54–77, doi: 10.1016/j.gca.2019.12.032.

Weis, F., 2013 Oxygen and iron isotope systematics of the Grängesberg mining district (GMD), Central Sweden Ph.D. dissertation, Uppsala University, Sweden (2013), p. 83

Wen, G., Li, J.-W., Hofstra, A.H., Koenig, A.E., Lowers, H.A., and Adams, D., 2017, Hydrothermal reequilibration of igneous magnetite in altered granitic plutons and its implications for magnetite classification schemes: Insights from the Handan-Xingtai iron district, North China craton: Geochimica et Cosmochimica Acta, v. 213, p. 255–270, doi: 10.1016/j.gca.2017.06.043.

Wilson, S., Koenig, A., and Lowers, H., 2012, A new basaltic glass microanalytical reference material for multiple techniques: Microscopy Today, v. 20, p. 12–16, doi: 10.1017/S1551929511001441.

Winchester, J.A., and Floyd, P.A., 1977, Geochemical discrimination of different magma series and their differentiation products using immobile elements: Chemical Geology, v. 20, p. 325–343, doi: 10.1016/0009-2541(77)90057-2.

Wu, C.C., and Mason, T.O., 1981, Thermopower measurement of cation distribution in magnetite: Journal of the American Ceramic Society, v. 64, p. 520–522, doi: 10.1111/j.1151-2916.1981.tb10317.x.

Xing, Y., Brugger, J., Etschmann, B., Tomkins, A.G., Frierdich, A.J., and Fang, X., 2021, Trace element catalyses mineral replacement reactions and facilitates ore formation: Nature Communications, v. 12, p. 1388, doi: 10.1038/s41467-021-21684-5.

Ye, H., Wu, C., Brzozowski, M.J., Yang, T., Zha, X., Zhao, S., Gao, B., and Li, W., 2020, Calibrating equilibrium Fe isotope fractionation factors between magnetite, garnet, amphibole, and biotite: Geochimica et Cosmochimica Acta, v. 271, p. 78–95, doi: 10.1016/j.gca.2019.12.014.

Yesavage, T., Stinchcomb, G.E., Fantle, M.S., Sak, P.B., Kasznel, A., and Brantley, S.L., 2016, Investigation of a diabase-derived regolith profile from Pennsylvania: Mineralogy, chemistry and Fe isotope fractionation: Geoderma, v. 273, p. 83–97, doi: 10.1016/j.geoderma.2016.03.004.

Yin, S., Wirth, R., He, H., Ma, C., Pan, J., Xing, J., Xu, J., Fu, J., and Zhang, X.-N., 2022, Replacement of magnetite by hematite in hydrothermal systems: A refined redox-independent model: Earth and Planetary Science Letters, v. 577, article 117282, doi: 10.1016/j.epsl.2021.117282.

Zhao, J., Brugger, J., and Pring, A., 2019, Mechanism and kinetics of hydrothermal replacement of magnetite by hematite: Geoscience Frontiers, v. 10, p. 29–41, doi: 10.1016/j.gsf.2018.05.015.

Brandon Sullivan earned his B.Sc. from Missouri University of Science and Technology in 2018 and completed undergraduate research focusing on the Viburnum Trend Mississippi Valley-type deposit in Missouri, USA. Following his undergrad career, Brandon went on to become a graduate student at Missouri S&T with research focusing on the mineral chemistry of Missouri's igneous-hosted Fe deposits, while also working part time as an intern at the Doe Run Company. Brandon transitioned to a full-time geologist position at the Doe Run Company in summer 2022 and is anticipated to graduate with his Ph.D. in spring of 2023.